

Vertical resolution of baroclinic modes in global ocean models



K.D. Stewart^{a,b,*}, A.McC. Hogg^{a,b}, S.M. Griffies^c, A.P. Heerdegen^{a,b}, M.L. Ward^d, P. Spence^{b,e},
M.H. England^{b,e}

^a Research School of Earth Sciences, Australian National University, Australia

^b Australian Research Council Centre of Excellence for Climate System Science, Australia

^c NOAA/Geophysical Fluid Dynamics Laboratory, Princeton, USA

^d National Computational Infrastructure, Australian National University, Australia

^e Climate Change Research Centre, University of New South Wales, Australia

ARTICLE INFO

Article history:

Received 3 November 2016

Revised 3 February 2017

Accepted 19 March 2017

Available online 22 March 2017

Keywords:

Vertical resolution

Baroclinic modal structure

High-resolution global ocean model

ABSTRACT

Improvements in the horizontal resolution of global ocean models, motivated by the horizontal resolution requirements for specific flow features, has advanced modelling capabilities into the dynamical regime dominated by mesoscale variability. In contrast, the choice of the vertical grid remains a subjective choice, and it is not clear that efforts to improve vertical resolution adequately support their horizontal counterparts. Indeed, considering that the bulk of the vertical ocean dynamics (including convection) are parameterized, it is not immediately obvious what the vertical grid is supposed to resolve. Here, we propose that the primary purpose of the vertical grid in a hydrostatic ocean model is to resolve the vertical structure of horizontal flows, rather than to resolve vertical motion. With this principle we construct vertical grids based on their abilities to represent baroclinic modal structures commensurate with the theoretical capabilities of a given horizontal grid. This approach is designed to ensure that the vertical grids of global ocean models complement (and, importantly, to not undermine) the resolution capabilities of the horizontal grid. We find that for z-coordinate global ocean models, at least 50 well-positioned vertical levels are required to resolve the first baroclinic mode, with an additional 25 levels per subsequent mode. High-resolution ocean-sea ice simulations are used to illustrate some of the dynamical enhancements gained by improving the vertical resolution of a 1/10° global ocean model. These enhancements include substantial increases in the sea surface height variance (~30% increase south of 40°S), the barotropic and baroclinic eddy kinetic energies (up to 200% increase on and surrounding the Antarctic continental shelf and slopes), and the overturning streamfunction in potential density space (near-tripling of the Antarctic Bottom Water cell at 65°S).

© 2017 Elsevier Ltd. All rights reserved.

1. Introduction

Ocean modelling is an exercise in subjective compromise. Model development involves the continual reconfiguration of the three-way balance between those processes deemed essential to resolve, those processes deemed acceptable to parameterize (along with the methods to do so), and finite computational resources. Each model configuration is specifically selected for the intended purpose of the ocean model and the dynamics of interest, and the model output must be interpreted judiciously. Models offer valuable insights into numerous and specific aspects of the ocean's circulation and role in Earth's climate, although the compromises of

model design mean that no single model can be a complete description of Earth's ocean.

Evidence of these compromises is perhaps nowhere more apparent than in the selection of spatial resolution (Griffies et al., 2000). The benefits of resolving the smallest length-scales are obvious: the inclusion of all fluid processes with a complete and mature energy cascade permits the exact closure of the energy budget (e.g., Gayen et al., 2013). On the other hand, the computational expense of resolving the smallest length-scales is prohibitive; the computational resources required for direct numerical simulation studies of laboratory scale circulations ($O(1) \text{ m}^3$ domain) are comparable with those of modern coupled climate models. Therefore, in order to obtain a useful, manageable ocean model, a line must be drawn as to a minimum dynamically-active length-scale and a model configuration selected. The art of ocean modelling is knowing where to draw this line.

* Corresponding author at: Research School of Earth Sciences, Australian National University, Australia.

E-mail address: kial.stewart@anu.edu.au (K.D. Stewart).

For the horizontal dimensions, the ubiquity of mesoscale eddies and their profound contributions to the ocean's kinetic energy (e.g., Ducet et al., 2000; Wunsch, 2007; McWilliams, 2008) and general circulation (e.g., Hallberg and Gnanadesikan, 2006; Chassignet and Marshall, 2007; Waterman et al., 2011) provide a natural principal objective for model horizontal grid spacing, and thus, resolution requirements. The rotating and stratified nature of the ocean means that the dominant spatial scales of mesoscale eddies is largely reflected by the first baroclinic Rossby radius of deformation, L_1 . Resolving the ocean processes and variability at the L_1 -scale extends the dynamical functionality of the model into a regime suitable for short-term forecasting and many operational applications, as well as mesoscale eddy-mean-flow interactions and the associated inverse cascade of energy. Thus, L_1 serves as a convenient target length-scale for the refinement of horizontal resolution, motivating efforts to ensure the horizontal grid spacing is some predetermined fraction of L_1 (e.g., Griffies and Treguier, 2013; Hallberg, 2013).

For the vertical resolution, no equivalent quantifiable principal objective exists. Studies examining the effects of altering vertical resolution demonstrate the fundamental influence it has on ocean circulation (e.g., Adamec, 1988; Weaver and Sarachik, 1990; Barnier et al., 1991), although these efforts are far less mature than their horizontal resolution counterparts. Additionally, there is no obvious indication that a given vertical grid is sufficient for representing the dynamics resolved by the horizontal grid. In other words, there is presently no way to determine whether dynamics that are resolved horizontally can be resolved vertically, meaning the efforts to refine the horizontal resolution up to and beyond the L_1 -scale are potentially being undermined by an inadequate vertical grid. Methodologies to ensure consistent vertical and horizontal resolution capabilities exist for atmospheric models (e.g., Lindzen and Fox-Rabinovitz, 1989; Roeckner et al., 2006), however such an approach for ocean models is yet to be formulated. Developing this methodology is the primary motivation for this paper. We aim to ascertain the vertical resolution requirements for ocean models that are based on the theoretical capabilities of the horizontal grid, and to use these requirements to guide the construction of a vertical grid that is at least as good as the horizontal grid.

In order to establish resolution requirements we must first consider the processes that we are attempting to resolve. Vertical velocities throughout the ocean interior ($w \approx O(10^{-5}) \text{ m s}^{-1}$) are typically 4–5 orders of magnitude smaller than their horizontal counterparts ($u, v \approx O(1) \text{ m s}^{-1}$); this is in part due to constraints imposed by Earth's rotation, the ocean stratification and the ocean's geometrical aspect ratio (Mahadevan, 2006; Thomas et al., 2007). Based on these typical background vertical velocities, maintaining a stable Courant number (C)¹ for horizontal grid spacings aimed at resolving L_1 ($\Delta x, \Delta y \sim O(10) \text{ km}$) calls for a vertical grid with typical spacing no less than Δz of $O(10) \text{ m}$. Arguably more dynamically important than the background geostrophic motion are specific, localized vertical flows, such as the rapid diurnal restratification of the surface mixed layer (e.g., Brainerd and Gregg, 1993; Bernie et al., 2005) or the convective sinking of dense overflows, exhibiting velocities reaching upwards of $O(10^{-3}) \text{ m s}^{-1}$ (e.g., Legg, 2012; Phillips and Bindoff, 2014). A vertical grid that is designed to be numerically stable for the background motions will not be adequate for these vitally important but highly-localized processes (often too localized to be resolved by the horizontal grid).

At present, the standard design of a vertical grid is one where the vertical grid spacing is a function of depth, with fine spac-

ing of $O(1-10) \text{ m}$ at the ocean surface and coarser spacing of $O(100) \text{ m}$ below the pycnocline, reflecting the current understanding of the different ocean processes at these depths (e.g., Treguier et al., 1996). Despite this effort to acknowledge the different dynamical regimes, neither the fine surface resolution nor coarse abyssal resolution are adequate for resolving the dominant vertical dynamics at either of these levels, requiring that these processes still be parameterized through enhanced vertical eddy viscosities and diffusivities, convective adjustment, and numerous surface- and bottom-intensified schemes. Indeed, this issue led Griffies and Treguier (2013) to hypothesize: "Physical parameterizations, more so than vertical coordinates, determine the physical integrity of a global ocean climate simulation." That is, the bulk of the oceanic vertical motions are parameterized. Bearing this in mind, we should now have a better sense for the primary purpose of the ocean vertical grid: it is not to necessarily resolve the vertical motions, but rather to resolve the vertical structure of the horizontal motions. Therefore, the objective for constructing a vertical grid is a function of the vertical complexity of the horizontal velocities. Characterizing this vertical complexity is fundamental to choosing the vertical grid.

Horizontal velocities can be expressed as a superposition of mutually orthogonal vertical eigenmodes. The vertical structure of the horizontal velocities will be at least as complicated as these eigenmodes. For the ocean, the shape of these eigenmodes form the basis functions of the baroclinic modes, and depends on the water depth and stratification, allowing them to be estimated from observations and global hydrography (e.g., Wunsch, 1997; Smith, 2007). The characteristic horizontal length-scale of the m -th baroclinic mode is reflected by the mode- m deformation radius, L_m . These deformation radii are largest for L_1 and decrease for higher baroclinic modes, meaning a given horizontal grid can only support the fundamental modal dynamics of a finite number of baroclinic modes. It follows that the vertical grid should be designed to resolve the baroclinic modal structure of the highest mode supported by the horizontal grid. For example, based on Hallberg (2013), an ocean model with $\sim 1/4^\circ$ horizontal resolution should have a vertical grid designed to resolve the vertical structure of at least the first baroclinic mode. Equivalent calculations for horizontal resolution requirements of higher baroclinic modes calls for the vertical grids of $\sim 1/10^\circ$ ocean models to be designed to resolve the vertical structure of the second baroclinic mode.

Following Chelton et al. (1998) and Ferrari et al. (2010), the baroclinic modal structure can be approximated with the Wentzel-Kramers-Brillouin method (WKB; detailed in Section 2). It is important to note that the presence of bottom topography, the free-surface, and non-uniform stratification violates the conditions for the strict validity of the WKB approximation (Hallberg and Rhines, 1996; Chelton et al., 1998), meaning the actual ocean horizontal velocity field is likely to be more complicated than the WKB method suggests. Also, topographic slopes and mean flows affect the baroclinic modal structure and are taken into account by the WKB method (e.g. Tailleux, 2003; Hunt et al., 2012). Nevertheless, the WKB approximation provides an indication of the lower limit of the complexity of the vertical structure of the horizontal flows, from which minimum requirements for the vertical resolution can be formulated. This approach has the advantage that the vertical grid can be tailored to the theoretical resolution capabilities of the horizontal grid; that is, if the horizontal grid is designed to resolve dynamics at the mode- m baroclinic deformation radius, this methodology ensures the vertical grid can do the same. Additionally, this methodology provides an objective means to quantify the ability of a given vertical grid to resolve baroclinic mode- m and directly compare this with other vertical grids.

The goals for this paper are twofold. Firstly, we introduce a methodology for objectively constructing (Section 2) and comparing (Section 3) vertical grids that is based on hydrography and

¹ Courant number $C = u\Delta t/\Delta x, v\Delta t/\Delta y$, and $w\Delta t/\Delta z$, where $\Delta x, \Delta y$ and Δz are the longitudinal, latitudinal and vertical grid spacings, respectively, and $\Delta t \approx 1800 \text{ s}$ is the model timestep typical of L_1 -scale global models.

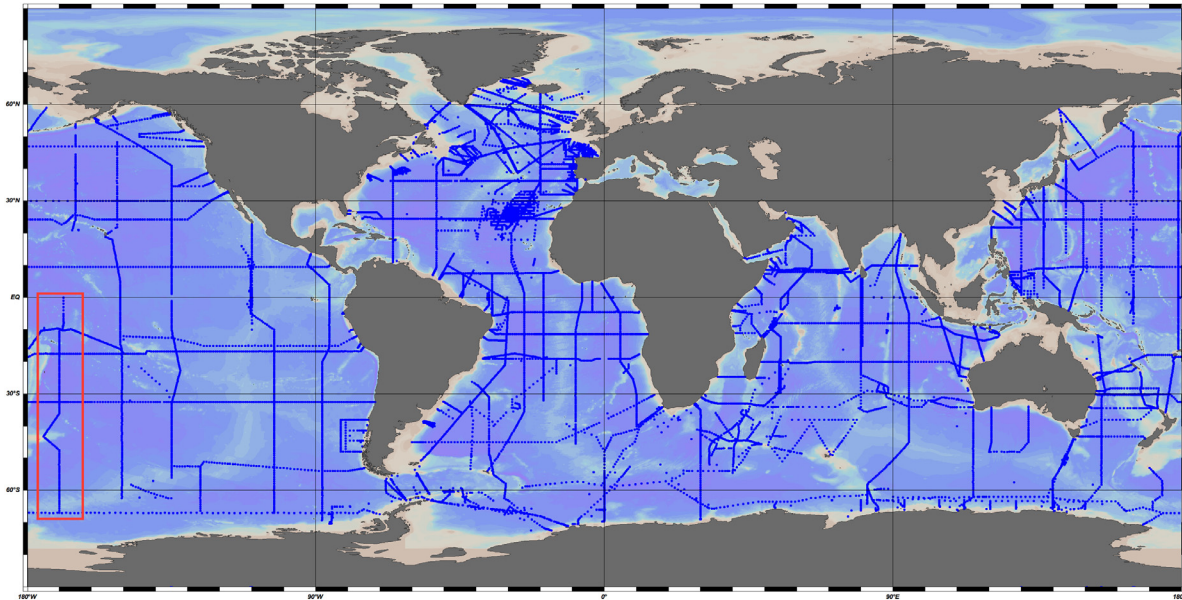


Fig. 1. A map for the locations of the ~18,000 CTD casts used here. The south Pacific section boxed in red is P15 used to generate the transects of Fig. 2. This image was generated with the Ocean Data View software program (Schlitzer, 2015). (For interpretation of the references to colour in this figure legend, the reader is referred to the web version of this article.)

theoretical resolution capabilities of the horizontal grid. Secondly, we illustrate some of the important dynamical benefits realised by improving vertical resolution in a $1/10^\circ$ global ocean model (Section 4). For the first goal, we employ observational hydrographic data to estimate a lower-bound for the vertical complexity of the horizontal flows. This estimate guides the development of minimum resolution requirements for a vertical grid that complements (and, importantly, does not undermine) the horizontal grid. Our approach suggests that at least 50 well-positioned vertical levels are required for a z -coordinate global ocean model to resolve the first baroclinic mode, with subsequent modes requiring at least an additional 25 levels each. For the second goal, we compare fundamental aspects of the global ocean circulations from two $1/10^\circ$ global ocean-sea ice simulations; one using a pre-existing 50 level vertical grid, and one using a new, objectively-constructed 75 level vertical grid. This comparison is designed to highlight the leading-order influence that vertical resolution has on the global circulation of a $1/10^\circ$ ocean model. We demonstrate that improving the vertical resolution for this level of horizontal resolution increases the sea surface height variability and eddy kinetic energy at all depths, especially near topography, facilitating an increase in deep-water formation and sinking and, subsequently, the global overturning circulation.

2. Constructing vertical grids for global ocean models

This section begins by detailing the approach to characterize the vertical structure of the ocean from global hydrography, and thereby establish the vertical resolution requirements of a given baroclinic mode. We then describe the technique for constructing the vertical grid to meet these resolution requirements, and finally develop a series of grids based on global hydrography.

2.1. Establishing vertical resolution requirements

2.1.1. Hydrographic data

To establish the vertical resolution requirements for global ocean models we must first determine the vertical complexity of horizontal flows in the global ocean. The baroclinic modal structure

of the global ocean provides a lower-bound estimate of this vertical complexity, and can be calculated from highly resolved profiles of ocean stratification. For this stratification we employ full-depth high-resolution profiles of *in situ* temperature and salinity from approximately 18,000 CTD casts of the World Ocean Circulation Experiment (WOCE, Fig. 1). These data were collected by 475 cruises between 1988 and 1998 and provide an almost global representation of ocean hydrography (although there is no data from the Arctic Ocean, Canadian Archipelago, Baffin Bay, or Greenland, Iceland and Norwegian Seas). The vertical grid spacing of these profiles is approximately 4 m on average, but is irregular and varies within and between casts, with a lower limit of 0.1 m, and an average of 712 data points per cast. For our purpose, these data are considered representative of the hydrography for the global ocean; establishing the vertical resolution requirements for regional ocean models should incorporate more localized hydrographic observations.

These data are downloaded from the Electronic Atlas of WOCE Data website (eWOCE; www.ewoce.org, Schlitzer, 2000). The Ocean Data View software program (ODV; Schlitzer, 2015) is used to initially explore the data and export potential temperature and salinity as a NetCDF file. Once in NetCDF form, the python implementation of the Gibbs SeaWater Oceanographic Toolbox TEOS-10 software package (GSW, version 3.0.3; IOC et al., 2010) is used to calculate the Conservative Temperature Θ ($^\circ\text{C}$) and Absolute Salinity S_A (g kg^{-1} ; Fig. 2a,b).

2.1.2. Determining the vertical complexity

The approach presented here is based on being able to characterize a minimum level of complexity for the vertical structure of the horizontal velocities. One such estimate of this minimum complexity is obtained using the WKB method for approximating baroclinic modes. A brief description of the WKB methodology is presented here; for a more complete review we refer to Chelton et al. (1998) and Ferrari et al. (2010), and references therein.

The squared buoyancy frequency N^2 (s^{-2} ; Fig. 2c) can be calculated from vertical profiles of Θ and S_A as,

$$N^2 = g \left(\alpha^\ominus \frac{\partial \Theta}{\partial z} - \beta^\ominus \frac{\partial S_A}{\partial z} \right), \quad (1)$$

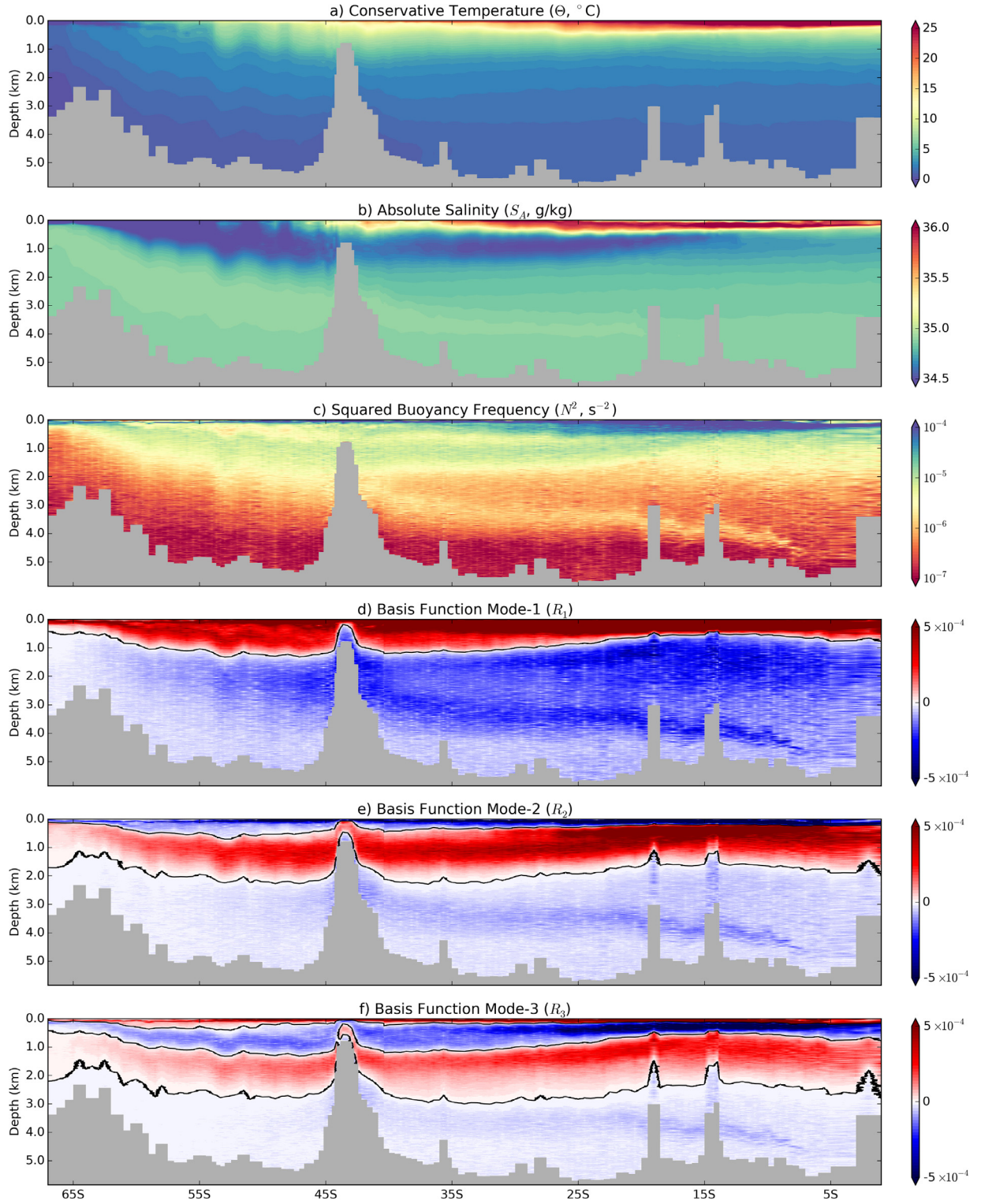


Fig. 2. Transects through the south-western Pacific (P15, approximately 170°W) of (a) Conservative Temperature Θ , (b) Absolute Salinity S_A , (c) squared buoyancy frequency N^2 , and (d–f) the basis functions R_m of the first 3 baroclinic modes. For (d–f), the modal zero crossings $h_{m,k}$ are contoured in black (recall there are a total of m zero crossings for mode- m). The shallowest mode-2 zero crossing in (e), $h_{2,1}$, is the term calculated for the 1/4° World Ocean Atlas 2013 and shown in Fig. 3. The large topographic feature to the north of 45°S is Chatham Rise.

where g (m s^{-2}) is the acceleration due to gravity, z is the depth (m, negative downwards, $z = 0$ at surface), and α^Θ ($^\circ\text{C}^{-1}$) and β^Θ (kg g^{-1}) are the thermal expansion and saline contraction coefficients, respectively, where the superscript Θ indicates these coefficients are calculated with the TEOS-10 (IOC et al., 2010).

From Chelton et al. (1998), the WKB approximation gives the mode- m baroclinic wavespeed, c_m (m s^{-1}), as a function of the depth-integrated buoyancy frequency,

$$c_m \approx \frac{1}{m\pi} \int_{-H}^0 N dz, \quad (2)$$

where H (with units m) is the ocean bottom depth, with $-H \leq z \leq 0$ the range for the vertical coordinate. Following Hallberg (2013), this wavespeed c_m can be used to estimate the deformation radius of the mode- m L_m as,

$$L_m = \sqrt{\frac{c_m^2}{(f^2 + 2\beta c_m)}}, \quad (3)$$

where f (s^{-1}) is the Coriolis parameter and $\beta = \partial f / \partial y$ ($m^{-1}s^{-1}$) is its meridional derivative. Expressed in this form the deformation radius remains latitudinally smooth across the Equator, unlike alternative definitions which require an arbitrary transition zone at low latitudes (e.g., Chelton et al., 1998). The mode- m baroclinic wavelength λ_m (with units m) is related to the mode- m deformation radius L_m by a factor of 2π , as,

$$\lambda_m = 2\pi L_m. \quad (4)$$

The horizontal grid spacings ($\Delta x, \Delta y$) of global ocean models are typically non-uniform and vary spatially (especially with latitude), making it convenient to represent the model horizontal resolution by the model effective horizontal grid spacing $\tilde{\Delta}$ (with units m; e.g., see Hallberg, 2013), given as,

$$\tilde{\Delta} = \sqrt{\frac{(\Delta x^2 + \Delta y^2)}{2}}. \quad (5)$$

Resolving the mode- m baroclinic wavelength with a discrete, non-spectral horizontal grid requires the model effective horizontal grid spacing to be,

$$\tilde{\Delta} \leq a \lambda_m, \quad (6)$$

where a is a scaling threshold that is no larger than $1/2\pi$ (e.g. Griffies and Treguier, 2013; Hallberg, 2013) or perhaps even smaller (e.g. Soufflet et al., 2016). That is, there needs to be at least 2π grid points per baroclinic wavelength. Taking this upper bound of $a = 1/2\pi$ we can rewrite Eq. (6) in terms of the baroclinic mode- m deformation radius, requiring the effective horizontal grid spacing $\tilde{\Delta}$ to be,

$$\tilde{\Delta} \leq L_m. \quad (7)$$

Irrespective of the exact value of a required for effective resolution, it is common practice to use the ratio $L_m / \tilde{\Delta}$ to compare the relative resolution capabilities of different horizontal grids.

From Ferrari et al. (2010), the buoyancy frequency and wavespeed are used to calculate the WKB approximation for $R_m(z)$, the non-dimensional basis function for the horizontal velocity of baroclinic mode- m , as,

$$R_m(z) \approx -\left(\frac{c_m N(z)}{g}\right) \cos\left(\frac{1}{c_m} \int_{-H}^z N(z) dz\right). \quad (8)$$

These basis functions R_m serve to estimate the minimum complexity of the vertical structure of the baroclinic mode- m horizontal velocity (Fig. 2d–f). Resolving the vertical structure of these modes is the primary purpose of the vertical grid, and knowledge of this modal structure provides guidance for constructing the vertical grid.

2.1.3. Resolving the modal structure

Resolving a baroclinic mode with a discrete vertical grid requires the vertical positions of the modal zero crossings, as well as the modal peaks and troughs, to be accurately represented. One can approach this exercise as if discretizing a continuous sine wave with a finite number of irregularly spaced points. Having at least six points per wavelength permits interpolation between points to locate peaks, troughs and zero crossings with functions of order greater than linear. Thus, here we require the vertical grid to have at least three grid points between modal zero crossings (indicated

by black contours in Fig. 2d–f), which is equivalent to having at least six points per wavelength. For each baroclinic mode- m there exist m zero crossings; here, we refer to the vertical position of the K -th zero crossing of the mode- m basis function as $h_{m,K}$ (with units m), defined to be negative, where $h_{m,1}$ is the shallowest zero crossing and $h_{m,m}$ is the deepest zero crossing of mode- m . To ensure that at least three grid points lie between the zero crossings at $h_{m,n}$ and $h_{m,n-1}$, the vertical grid spacing at vertical position $h_{m,n}$ must be at most one-third of the distance between these zero crossings. That is, the vertical grid spacing Δz at position $h_{m,n}$ is,

$$\Delta z(h_{m,n}) \leq \frac{h_{m,n-1} - h_{m,n}}{3}. \quad (9)$$

Additionally, the criterion for at least three grid points between zero crossings also applies at the ocean bottom H and the surface,

$$\Delta z(H) \leq \frac{h_{m,m} + H}{3} \quad \& \quad \Delta z(h_{m,1}) \leq \frac{-h_{m,1}}{3}. \quad (10)$$

These requirements provide upper bounds for Δz as a function of the zero crossing vertical positions. That is, these constraints provide a set of positions ($h_{m,K}$) and the largest spacing that the vertical grid can be at these positions ($\Delta z(h_{m,K})$) in order to resolve baroclinic mode- m . These resolution requirements ($h_{m,K}, \Delta z(h_{m,K})$) guide the construction of the vertical grid, and they can be tailored to match the mode- m resolution capabilities of a given horizontal grid.

Fig. 3 is a visual representation of the field $h_{m,K}$, offering insight into the relative vertical resolution requirements for different regions: where $h_{m,K}$ is shallow (deep), the vertical grid spacing should be relatively small (large). It depicts the spatial distribution of the shallowest mode-2 zero crossing position, $h_{2,1}$, developed from the climatological annual mean temperatures and salinities of the 1/4° World Ocean Atlas 2013 (WOA13; Locarnini et al., 2013; Zweng et al., 2013). It is initially obvious that this field is smallest in shallow regions (on continental shelves and plateaus). The $h_{2,1}$ zero crossing is also shallow in regions associated with relatively strong stratification (e.g., low latitudes and polar regions). These are regions where the vertical structure and complexity of the horizontal flows tend to be concentrated towards the upper ocean, requiring finer vertical grid spacing to resolve their dynamics. Regions where $h_{2,1}$ is deeper (midlatitude gyres, subpolar North Atlantic and the Antarctic Circumpolar Current) are regions typically associated with low mode- m baroclinic flows. Interestingly, there is no evidence of the strong latitudinal dependence observed in equivalent figures relating to the horizontal resolution requirements (e.g., Fig. 1 of Hallberg, 2013). Instead, the factors with the greatest influence on $h_{m,K}$ (and thus the vertical resolution requirements for modal structures) are the ocean depth and stratification, with the latter indicating a seasonal dependence to the vertical resolution requirements. Note that this seasonality of the stratification suggests finer resolution requirements during the summer, implying that the summer-biased observations of high latitudes will tend to over-estimate the vertical resolution requirements for other times of the year. The regional variations of $h_{m,K}$ is not conducive to a globally prescribed vertical grid, meaning a global ocean model will require a higher number of vertical levels than its regional counterpart.

2.2. Constructing a vertical grid

The exercise now is to develop a vertical grid guided by the findings from Section 2.1. Following Treguier et al. (1996), this grid will have smoothly-varying vertical grid spacing that increases monotonically with depth. Constructing the grid is not trivial and it is useful to consider this exercise as a sequence of distinct steps, each relating to different aspects of the vertical grid. A convenient

World Ocean Atlas 2013: $h_{2,1}$

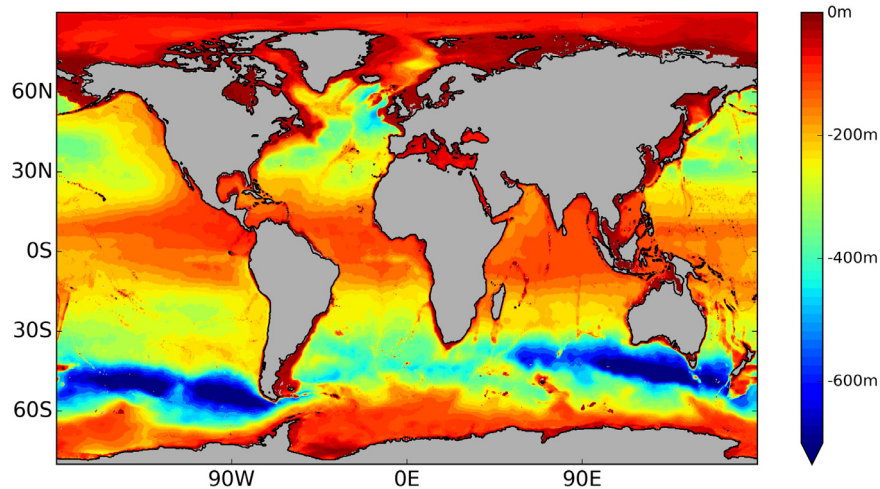


Fig. 3. The vertical position of the shallowest mode-2 zero crossing ($h_{2,1}$), calculated from the climatological annual mean of temperatures and salinities from the 1/4° World Ocean Atlas 2013. This field is representative of the relative vertical resolution requirements of the mode-2 dynamics; where $h_{2,1}$ is shallow (deep), the required vertical grid spacing refines (coarsens). The factors with the greatest influence on $h_{m,k}$ (and thus the resolution requirements) are the ocean depth and stratification.

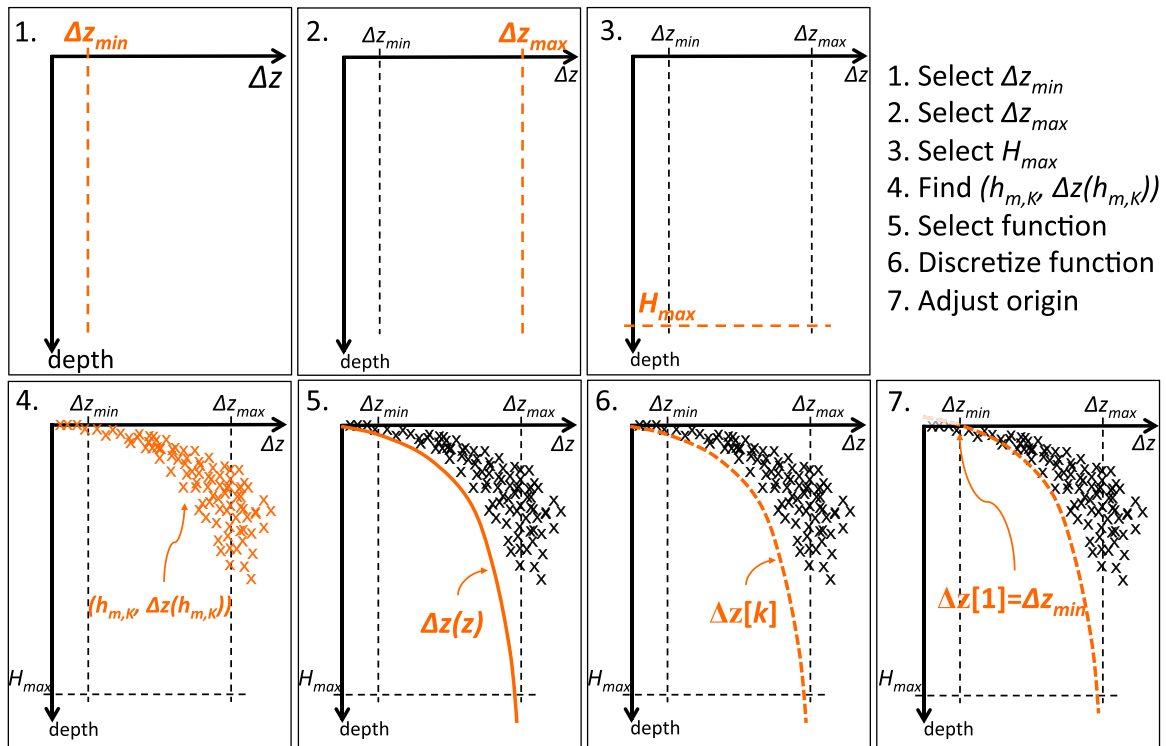


Fig. 4. A schematic depicting the steps used here to build the vertical grids, as detailed in Section 2.2. The item of interest for each step is shown in orange. The step to discretize the function (#6) is expanded upon in Fig. 5. (For interpretation of the references to colour in this figure legend, the reader is referred to the web version of this article.)

representation of the vertical grid is the $(z, \Delta z)$ -space, which we use to schematically depict the steps for constructing a vertical grid (each step below being explicitly represented in Fig. 4).

1. Select the surface grid spacing: Δz_{min}

We begin by selecting the vertical grid spacing at the ocean surface. This will be the minimum vertical grid spacing and is referred to as Δz_{min} (Fig. 4, panel 1). The selection of Δz_{min} is predominantly based on surface processes of interest, such as surface fluxes, the diurnal radiation and/or surface mixed-layer restratification cycles (e.g., Brainerd and Gregg, 1993; Bernie

et al., 2005), rather than the ability of the vertical grid to resolve a given baroclinic mode. Leading global ocean models presently have $\Delta z_{min} = O(1)$ m (Hewitt et al., 2016), which is where we base our selection of surface grid spacing.

2. Select the abyssal grid spacing: Δz_{max}

The next decision is the vertical grid spacing for the abyssal ocean. As the vertical grid spacing increases monotonically with depth, the abyssal grid spacing Δz_{max} represents the coarsest vertical resolution in the domain (Fig. 4, panel 2). Dynamics to consider when selecting Δz_{max} include the representation of dense abyssal overflows (e.g., Legg, 2012), bottom-trapped to-

pographic Rossby waves (e.g., Rhines, 1970), and lee waves and tidal generated waves (e.g., Melet et al., 2014; Naveira Garabato et al., 2004). Another consideration is the grid aspect ratio (vertical-to-horizontal grid spacings, which bounds the topographic slope angle) and how this relates to typical critical angles for internal gravity waves (e.g., MacKinnon et al., 2013). It is important to note that Δz_{\max} is the grid spacing at the ocean bottom only where the model ocean is deepest; in shallower regions, such as on continental shelves, slopes, and oceanic ridges, the vertical grid spacing at the ocean bottom is less than Δz_{\max} . Also, the use of partial bottom cells (e.g., Adcroft et al., 1997; Pacanowski and Gnanadesikan, 1998) means the bottom-most cell is not constrained to be Δz_{\max} nor one of the pre-allocated Δz values. This added flexibility is designed to assist in the representation of bottom dynamics, and, in general, is not expected to enhance the ability of a given vertical grid to resolve the baroclinic modal structure. Therefore, for the purposes here, we are not considering the effects of partial bottom cells (although they are included in the global simulations detailed in Section 4). Following the lead of present global ocean models ($\Delta z_{\max} = 200\text{--}250$ m), we select $\Delta z_{\max} = O(100)$ m as our abyssal grid spacing.

3. Select the maximum ocean depth: H_{\max}

The maximum depth of the model ocean, here referred to as H_{\max} (Fig. 4, panel 3), is a decision likely determined by the quality of the bathymetric dataset and the importance of deep and abyssal watermasses to the processes of interest. In selecting H_{\max} one should be wary of opting to go too shallow. Ocean regions deeper than H_{\max} are truncated and represented in the model as flat plains of depth H_{\max} . Such topographic truncation can occupy large regions; typically, these include the Aleutian, Admundsen, Argentine, Bellingshausen, Ceylon, Enderby and Weddell Basins. The dynamical consequences of this truncation should not be overlooked; without bathymetric features the deep eddy energy becomes isotropic and behaves as f -plane turbulence, unlike the typical strongly anisotropic bottom variability that aligns with f/H contours (Stewart et al., 2015). Additionally, the capacity of the ocean volume beneath H_{\max} to store heat is absent from models, which presents a problem for long-term climate simulations with relatively shallow oceans. Leading global ocean models employ H_{\max} values approaching ~ 6000 m (Hewitt et al., 2016), which we adopt here.

4. Select the target baroclinic mode- m and establish resolution requirements: $(h_{m, \kappa}, \Delta z(h_{m, \kappa}))$

Once the values for Δz_{\min} , Δz_{\max} and H_{\max} have been selected, we need to decide on the highest baroclinic mode that we are attempting to resolve. This decision will largely be based on the resolution capabilities of the horizontal grid, i.e. the largest mode- m for which the ratio $L_m/\bar{\Delta}$ is acceptable (e.g., Hallberg, 2013). Upon deciding this mode- m , we obtain the baroclinic mode- m resolution requirements as per Section 2.1. It is useful to represent these requirements in a paired format comprising a zero crossing vertical position, $h_{m, \kappa}$, and the upper limit of vertical grid spacing for this position, $\Delta z(h_{m, \kappa})$. The global set of these pairs $(h_{m, \kappa}, \Delta z(h_{m, \kappa}))$ are depicted schematically in Fig. 4 panel 4 for $(z, \Delta z)$ -space. The set of pairs $(h_{m, \kappa}, \Delta z(h_{m, \kappa}))$ tend to populate a coherent region with an upper bound at $\Delta z(z = h_{m, 1}) = -h_{m, 1}/3$ (from Eq. (10)). Representing these resolution requirements in this way provides guidance for constructing the vertical grid: in order to meet the requirements of Section 2.1, the vertical profile of grid spacing with depth must lie to the left of all pairs $(h_{m, \kappa}, \Delta z(h_{m, \kappa}))$ in $(z, \Delta z)$ -space.

5. Select a functional form: $\Delta z(z)$

The next step is to select a smooth functional form for $\Delta z(z)$ (Fig. 4, panel 5). The chosen function must cross through $z = 0$ at some small positive value $\Delta z(0) = \epsilon$ where $0 < \epsilon \leq \Delta z_{\min}$

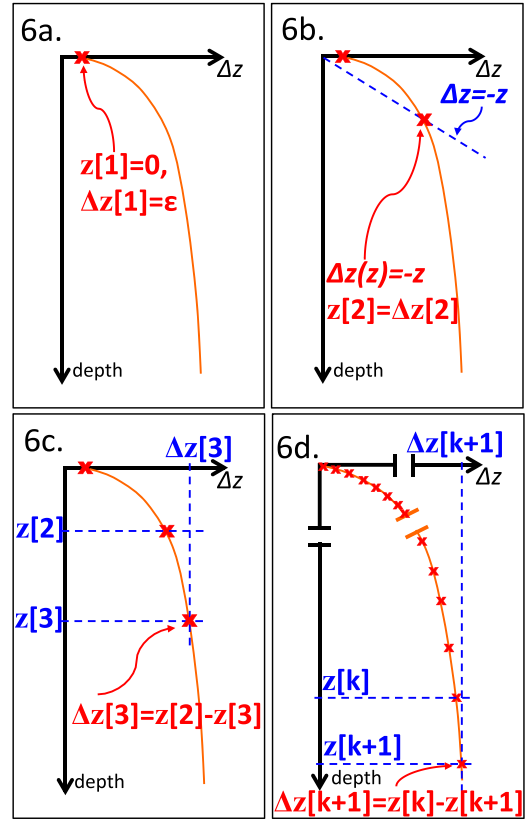


Fig. 5. Step #6 of Section 2.2 is the discretization of the analytical function for the vertical grid spacing with depth, $\Delta z(z)$ (Eq. (11)). This step is broken into four steps, 6a–d.

(the reason for this $\Delta z(0) = \epsilon$ requirement becomes apparent in the discretization step); note that for this step it is not necessary to require that $\Delta z(0) = \Delta z_{\min}$. At depth, the chosen function will tend smoothly towards Δz_{\max} as it approaches H_{\max} , and discontinuities in $\Delta z(z)$ must be avoided for all depths (see Treguier et al., 1996). The function should lie to the left of the $(h_{m, \kappa}, \Delta z(h_{m, \kappa}))$ pairs in $(z, \Delta z)$ -space.

For the purposes here, and the global eWOCE data described in Section 2.1, it is apparent that a hyperbolic tangent would satisfy the mode-1–3 resolution requirements; however, when developing vertical grids for specific regions or for targeting higher-order baroclinic modes, alternative functional forms may be preferable. The function employed here is (recall $-H_{\max} \leq z \leq 0$),

$$\Delta z(z) = \Delta z_{\max} \tanh\left(\frac{-z\pi}{s_h H_{\max}}\right) + \epsilon, \quad (11)$$

where s_h (≈ 1.0) is a dimensionless scaling parameter for adjusting the “knee”-depth of the hyperbolic tangent (i.e. increasing s_h steepens the profile). Here we use $\epsilon = 10^{-3}$ m.

6. Discretize the vertical grid: $\Delta z[k]$

Once a smooth continuous function for $\Delta z(z)$ has been selected, it needs to be discretized into a pair of vectors $\mathbf{z}[\cdot]$ and $\Delta \mathbf{z}[\cdot]$, the lengths of which are not prescribed. This process is not trivial and involves an iterative procedure (Fig. 5):

- Discretizing the vertical grid begins at the surface where we already know $z = 0$ and $\Delta z(0) = \epsilon$. These values form the first entries in the vectors $\mathbf{z}[\cdot]$ and $\Delta \mathbf{z}[\cdot]$, respectively, so that $z[1] = 0$ and $\Delta z[1] = \epsilon$ (Fig. 5a).
- The second entries in the $\mathbf{z}[\cdot]$ and $\Delta \mathbf{z}[\cdot]$ vectors occur at the point where $\Delta z(z) = -z$ (Fig. 5b). The criteria that $\Delta z(0) = \epsilon > 0$ and $\Delta z(H_{\max}) < H_{\max}$ means the func-

tion $\Delta z(z)$ must intersect the line $-z = \Delta z$ for some value of z . For the function employed here, this value can be determined analytically from Eq. (11), such that $z[2] = -\Delta z[2]$.

- (c) Calculating the third entries of $\mathbf{z}[\cdot]$ and $\Delta\mathbf{z}[\cdot]$ is more complicated. From the vertical position of $z = z[2]$, we gradually step along the function until we reach a position z^\dagger , where

$$\Delta z(z^\dagger) = z[2] - z^\dagger. \quad (12)$$

This procedure can be automated to satisfy the expression:

$$\Delta z(z^\dagger) - z[2] + z^\dagger = 0. \quad (13)$$

Once this expression is satisfied, z^\dagger and $\Delta z(z^\dagger)$ become the values for $\mathbf{z}[3]$ and $\Delta\mathbf{z}[3]$, respectively, such that $\Delta z[3] = z[2] - z[3]$ (Fig. 5c).

- (d) Subsequent entries for $\mathbf{z}[\cdot]$ and $\Delta\mathbf{z}[\cdot]$ follow on from the procedure to calculate $\mathbf{z}[3]$ and $\Delta\mathbf{z}[3]$. From each vertical position $\mathbf{z}[k]$, we step along the function to a position z^\dagger that satisfies the expression:

$$\Delta z(z^\dagger) - z[k] + z^\dagger = 0. \quad (14)$$

These subsequent values of z^\dagger and $\Delta z(z^\dagger)$ become $z[k+1]$ and $\Delta z[k+1]$, respectively, continuing the sequence (Fig. 5d),

$$\Delta z[k+1] = z[k] - z[k+1]. \quad (15)$$

This iterative process continues until the depth of $\mathbf{z}[k]$ surpasses the maximum depth H_{\max} and the procedure is terminated. Note that the number of iterations required for $\mathbf{z}[\cdot]$ to reach H_{\max} is not prescribed.

7. Adjust the origin for: $\Delta z[1] = \Delta z_{\min}$

Once the function is discretized beyond the depth H_{\max} , attention is returned to the top of the $\mathbf{z}[\cdot]$ and $\Delta\mathbf{z}[\cdot]$ vectors. Initially, for the purposes of discretization we prescribed $\Delta z[1] = \epsilon$, however we would prefer $\Delta\mathbf{z}[1]$ to be closer to Δz_{\min} . For this purpose we search through the $\Delta\mathbf{z}[\cdot]$ vector to identify the largest entry satisfying $\Delta z[\cdot] < \Delta z_{\min}$. Entries prior to this, and their corresponding entries in the $\mathbf{z}[\cdot]$ vector, are then removed, effectively adjusting the origin of the grid such that $z[1] = 0$ and $\Delta z[1] \approx \Delta z_{\min}$ (Fig. 4, panel 7). Occasionally, this vertical shift reduces the maximum depth of the vertical grid to an undesired depth, in which case it is useful to recommence the iterative stepping until $z[k] < -H_{\max}$ is again surpassed.

This algorithm does not prescribe a total number of vertical levels. Rather, the total number of levels is a derived quantity that is controlled by the choices of Δz_{\min} , Δz_{\max} , H_{\max} , the functional form of the vertical grid, and the number of baroclinic modes to be resolved. In the event that the iterative process returns an unacceptable number of levels, one or more of these factors must be adjusted and the algorithm repeated.

2.3. Vertical grids based on global hydrography

Here, we construct four vertical grids with varying resolution capabilities based on the modal structure of the first three baroclinic modes. These are referred to as KDS50, KDS65, KDS75 and KDS100, indicative of the number of vertical levels in each grid. The KDS50 and KDS75 are developed for comparison with existing 50 and 75 level z -coordinate ocean grids, and target the baroclinic modes $m = 1$ and $m = 2$, respectively. KDS65 is designed so as to have the modal structure resolution capabilities of the leading existing 75 level grid but with the least number of levels possible. The KDS100 is presented as a high-resolution option that extends the existing mode-1 resolution capabilities to mode-3.

From the eWOCE data described in Section 2.1, the vertical profiles of Conservative Temperature Θ and Absolute Salinity S_A are used to calculate the squared buoyancy frequency N^2 as per Eq. (1). Representative transects of the Θ , S_A and N^2 fields from the south-western Pacific Ocean (WOCE Section P15) are presented in Fig. 2a–c. The bulk of the Θ and S_A structure is concentrated in the upper 1000m where N^2 is largest. Beneath this depth the Θ and S_A fields are comparatively homogeneous and N^2 is small.

This vertical partition in strength of the stratification is reflected by the zero crossing $h_{1,1}$ depth of the first baroclinic mode basis function R_1 (black contour of Fig. 2d). This mode-1 basis function and zero crossing exhibits a horizontal coherence, with the largest variation associated with major topographic features (e.g., near Chatham Rise, $\sim 20^\circ\text{S}$ and $\sim 15^\circ\text{S}$). The spatial coherence remains evident in the basis functions of the higher modes (Fig. 2e–f). For modes $m = 2$ and $m = 3$, the shallower zero crossings exhibit less variance than their deeper counterparts. Again, the largest variations of $h_{m,K}$ are located in regions near major topographic features.

The depths of $h_{m,K}$ and H (contours and bathymetry of Fig. 2d–f) are calculated as well as the vertical distances separating them. These values are used in Eqs. (9) and (10) to define the vertical grid spacings Δz at $h_{m,K}$ and H necessary to ensure there are at least three grid points between zero crossings. Each pair of $(h_{m,K}, \Delta z(h_{m,K}))$ are plotted in $(z, \Delta z)$ -space for the baroclinic modes 1–3 (Fig. 6). Also shown are profiles of the vertical grid spacing for the nine vertical grids examined here. These are the four new, objectively-constructed KDS-series vertical grids, and five pre-existing vertical grids of global z -coordinate models with effective horizontal grid spacings smaller than $1/10^\circ$: the 51 level Ocean Forecasting Australia Model grid (OFAM; Oke et al., 2012); the 46 and 75 level grids developed by the DRAKKAR consortium (The DRAKKAR Group, 2007) for the Nucleus for European Modelling of the Ocean platform (NEMO; Madec, 2008); the 50 level grid developed by the NOAA/GFDL for use with the Modular Ocean Model version 5 (MOM5; Delworth et al., 2012; Griffies et al., 2015); and the 90 level grid recently developed for the LLC hierarchy of global ocean-sea ice simulations (where LLC refers to latitude-longitude-polar cap; e.g., Rocha et al., 2016) using the MIT-gcm (Marshall et al., 1997; Hill et al., 2007). These pre-existing grids are referred to here as OFAM51, NEMO46, NEMO75, GFDL50, and LLC90, respectively. As a qualitative test of whether a vertical grid meets the resolution requirements set out in Section 2.2 for a given baroclinic mode- m (i.e., having at least three grid points between zero crossings of mode- m globally), its vertical grid spacing profile must lie to the left (smaller Δz) of the data points in Fig. 6. Points in Fig. 6 that lie to the left of a given vertical grid spacing profile represent locations where that particular vertical grid has less than three grid cells between modal zero crossings; these locations predominantly occur in shallow regions (especially continental shelves) where particularly high vertical resolution is needed. It is interesting to note how well the vertical grid spacing profiles of the pre-existing vertical grids reflect the general form of the resolution requirements of Section 2.2, in spite of having been developed without these objective requirements in mind. From Fig. 6a, it is apparent that at least 50 well-positioned vertical levels are required to meet the resolution requirements of Section 2.2 for the first baroclinic mode.

3. Comparing vertical grids

The direct comparison of vertical grids in ocean models is not a trivial task. Traditionally, sensitivity studies compare a suite of model configurations run with a range of resolutions, and evaluate the influence of resolution based on the presence, absence, or characteristics of specific flow features (e.g., Adamec, 1988; Weaver

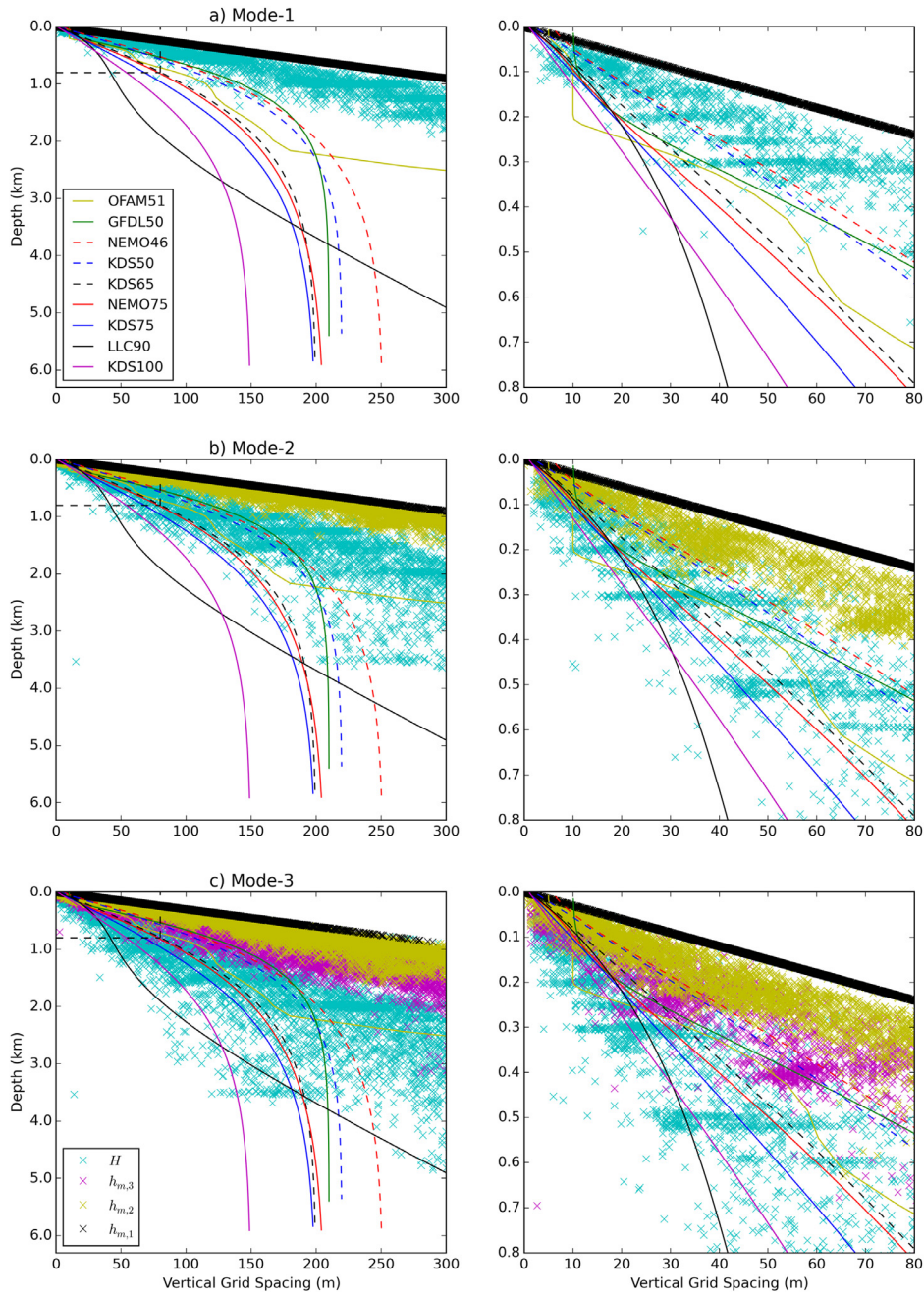


Fig. 6. The grid spacing Δz requirements given by Eqs. (9) & (10) for baroclinic mode-1 (a), mode-2 (b), and mode-3 (c). The maximum grid spacing permitted at the ocean bottom H is shown in cyan, at $h_{m,1}$ in black, at $h_{m,2}$ in yellow, and at $h_{m,3}$ in magenta. Profiles of the vertical grid spacing for the GFDL, NEMO, LLC and KDS grids are included for reference. The left column shows the full depth; the right focuses on the upper 800 m. Note the abscissa limits (300 & 80 m) omit deeper regions where $\Delta z(H)$ is off-scale; this is less of an issue for the higher modes where $\Delta z(H)$ is smaller. (For interpretation of the references to colour in this figure legend, the reader is referred to the web version of this article.)

and Sarachik, 1990). Here, we are attempting to compare the relative capabilities of different vertical grids to resolve the vertical structure of horizontal flows in state-of-the-art global ocean models. This structure is influenced by the ocean stratification and bathymetry, both of which depend on the vertical resolution itself. Additionally, a representative level of complexity in the vertical structure requires a richness of bathymetry that can only be achieved with a global ocean model domain. The practicalities involved in setting up a dynamic test to compare a suite of vertical grids are prohibitive. Instead, here we adopt a hierarchical approach to comparing vertical grids. The first stage is a static test that quantifies and compares the ability of several vertical grids to

resolve the baroclinic modal structures estimated from global hydrographic data. The second stage uses a $1/10^\circ$ global ocean-sea ice model to assess the dynamical benefits of employing an improved vertical grid (Section 4).

3.1. Methodology

We begin with a static test that uses the aforementioned eWOCE hydrographic data (Section 2.1) to estimate a lower bound of complexity for the vertical structure of the horizontal velocity field. The high-resolution fields for Θ , S_A and basis functions R_m^{WOCE} are developed from the eWOCE hydrography. These eWOCE fields

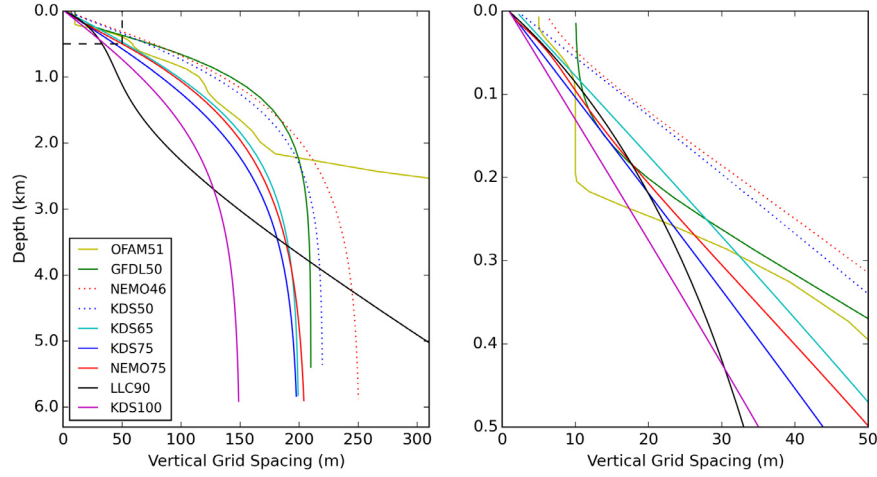


Fig. 7. Profiles of the vertical grid spacing Δz with depth for the grids developed and compared here. The boxed region in the left panel is expanded upon the right panel.

remain at the unstructured locations of the hydrographic data; this high-resolution, irregular-spacing of the CTD data is important because regularly spaced or gridded data (such as the WOA13) does not provide an unbiased hydrography field, and comparisons to it are overly influenced by the vertical grid of the hydrography and its resemblance to the test grid, as opposed to the hydrographic data itself. The Θ and S_A hydrographic data are then linearly interpolated onto the test vertical grids, where the test basis functions are calculated, and then compared with the eWOCE basis functions.

This procedure uses the methodologies of Eqs. (1), (2) & (8) to calculate the basis functions R_m for the first 3 baroclinic modes of each cast interpolated onto the test grids. The depths of the $m = 1-3$ modal zero crossings are noted for comparison with the eWOCE zero crossing depths and other test grids. The test basis functions are then re-interpolated back onto the eWOCE cast data levels for a direct comparison with the eWOCE fields. The global mean relative errors of the basis functions, $\overline{E(R_m)}$, and zero crossing depths, $\overline{E(h_{m,K})}$, for each mode $m = 1-3$ are calculated and compared for the different test grids. These two errors quantify the vertical interpolation errors of the mode- m basis functions and zero crossing depths, respectively. The first is calculated as the thickness weighted average of the difference between the test basis functions R_m and the eWOCE basis functions R_m^{WOCE} as,

$$\overline{E(R_m)} = \sqrt{\frac{\sum [(R_m - R_m^{WOCE})^2 \Delta z]}{\sum \Delta z}}. \quad (16)$$

The second is the global average of the absolute difference between the test $h_{m,K}$ and eWOCE $h_{m,K}^{WOCE}$ zero crossings, normalized by the eWOCE zero crossing,

$$\overline{E(h_{m,K})} = \frac{\overline{|h_{m,K} - h_{m,K}^{WOCE}|}}{\overline{|h_{m,K}^{WOCE}|}}. \quad (17)$$

Here, this static test is used to compare the four new grids developed with Section 2, and five others obtained from pre-existing configurations of global z-coordinate ocean models (Fig. 7, Table 1).

3.2. Resolving the modal structures from hydrography

From Fig. 6, further analysis could be conducted to quantify how well a given vertical grid meets the Section 2.2 resolution requirements for each mode (i.e., having at least three grid points between zero crossings of mode- m globally), perhaps by some metric that describes the fraction of points either side of the vertical grid

spacing profile. However, considering that the ultimate purpose for these grids is for use in global ocean models, it is more oceanographically relevant to assess how well a given grid can resolve the vertical structure of the ocean circulation. For this we use the Θ and S_A data from the CTD casts in Section 3.1; these are first linearly interpolated onto the various vertical grids, where the basis functions R_m of the baroclinic modes are calculated. These gridded R_m fields are then linearly re-interpolated back to the depths of the eWOCE data and compared with the eWOCE fields R_m^{WOCE} . The global-average relative error of the R_m for the first three baroclinic modes is calculated by Eq. (16) for each of the test vertical grids (Table 1, Fig. 8a). This calculation provides a bulk, robust measure of how well the vertical grid can resolve the horizontal velocity fields predicted by the WKB approximation. In general, increasing the number of vertical levels reduces the relative error, which makes physical sense. It is also apparent that vertical locations of the levels has a strong influence on the relative error; $\overline{E(R_m)}$ of the OFAM51 grid is substantially greater than those of the GFDL50, NEMO46 and KDS50 grids despite a similar number of vertical levels. However, when the calculation of $\overline{E(R_m)}$ is limited to the upper 250 m (where the OFAM51 grid preferentially stacks levels to improve representation of upper ocean processes), the relative error of the OFAM51 grid is smaller than the other ~ 50 level grids (Fig. 8b). The KDS65, designed to be as good as the existing 75 level grids but with less levels, is comparable with NEMO75 for the full-depth calculation of $\overline{E(R_m)}$, however returns a slightly higher relative error in the upper 250 m, presumably due to the difference in surface resolution (KDS65 minimum $\Delta z_{\min} = 2.3$ m versus NEMO75 at $\Delta z_{\min} = 1.0$ m). The highest resolution of the pre-existing vertical grids, LLC90, exhibits the least error of grids presently in use. The progressive reduction in full-depth $\overline{E(R_m)}$ from KDS50 through KDS75 to KDS100 suggests that for objectively-constructed vertical grids, approximately 25 additional levels are required in order for a given grid to resolve mode- $m + 1$ at least as well as it resolves mode- m .

An additional metric for comparing the vertical grids is the relative error of the zero crossing depths $\overline{E(h_{m,K})}$ (Eq. (17); Fig. 8c). This is a measure of the ability of the grid to identify specific depths important to the hydrography and flow dynamics (e.g., the $h_{1,1}$ zero crossing of Fig. 2d is a breakpoint in stratification strength, and closely related to the pycnocline). As with the $\overline{E(R_m)}$ metric, in general, increasing the number of vertical levels reduces $\overline{E(h_{m,K})}$, and the vertical positioning of the levels also has an influence.

Table 1
The vertical grids constructed and compared here.

Vertical Grid	Δz_{\min} (m)	Δz_{\max} (m)	H_{\max} (m)	$\overline{E(R_1)}$	$\overline{E(R_2)}$	$\overline{E(R_3)}$
KDS50	2.7	219.6	5363.5	0.394	0.432	0.453
KDS65	2.3	199.1	5820.9	0.358	0.396	0.419
KDS75	1.1	197.6	5836.6	0.346	0.384	0.408
KDS100	1.0	148.8	5912.4	0.310	0.346	0.370
OFAM51	5.0	906.1	4509.2	0.490	0.542	0.562
GFDL50	10.0	209.9	5395.0	0.395	0.431	0.454
NEMO46	6.4	250.2	5875.1	0.411	0.449	0.470
NEMO75	1.0	204.0	5902.1	0.352	0.390	0.414
LLC90	1.0	479.8	6760.2	0.329	0.365	0.390

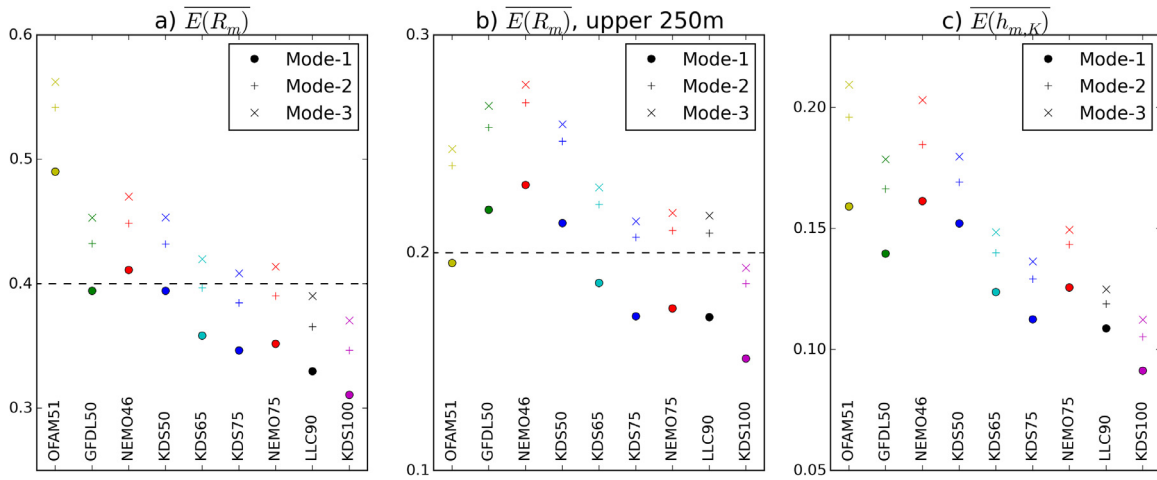


Fig. 8. The (a) full-depth and (b) upper 250 m global-averaged relative error of the first 3 baroclinic basis functions $\overline{E(R_m)}$ calculated for the different grids. The dashed lines are included for reference and comparison at a relative error of 0.4 and 0.2; these are not intended to indicate a resolution threshold value. The (c) global-averaged relative error of the shallowest modal zero crossing depths $\overline{E(h_{m,K})}$.

It is important to note that the two metrics presented here for comparing vertical grids ($\overline{E(R_m)}$ and $\overline{E(h_{m,K})}$) do not provide a threshold value or quantify whether a given baroclinic mode- m is resolved by a vertical grid. That said, neither do the traditional methods for evaluating the resolution capabilities of horizontal grids (e.g., Eqs. (6) & (7)). They do, however, provide a hydrographically-relevant comparison of vertical grids, enabling one to objectively gauge the relative benefits of various vertical grids, and assist in finding the balance between resolving, parameterizing and computing.

4. Improving the vertical resolution of a $1/10^\circ$ global ocean model

The intended purpose for the vertical grids developed and compared here is for use in state-of-the-art global ocean models. Thus, the ideal test of these grids requires circulations with the level of sophistication and complexity only provided by high-resolution global simulations. For such a test, it is essential that the horizontal grid supports the higher-order dynamics needed to distinguish the effects that the vertical grids have on the model circulation. For the $O(50-75)$ level grids examined here, the appropriate horizontal resolution is certainly no coarser than $1/10^\circ$, which will have regions that permit baroclinic mode-2 dynamics. The computational expense of a sensitivity study to compare this suite of vertical grids with a $1/10^\circ$ global ocean model is prohibitive. Therefore, rather than a complete dynamic investigation of the nine vertical grids here, we take this opportunity to examine the effects of improving vertical resolution in global ocean models by comparing two simulations: one using a pre-existing 50 level grid (GFDL50) and one with a new, objectively-constructed 75 level grid (KDS75). The (Δz_{\min} , Δz_{\max} , H_{\max}) values for the GFDL50 and KDS75 grids are

(10.0, 209.9, 5395.0) and (1.1, 197.6, 5836.6), respectively (Table 1). These two model simulations are configured to be identical in every way (including their timestep) apart from their vertical grid resolution.

Model description

The model is a global ocean-sea ice configuration of the MOM5 (Griffies, 2012) coupled with the GFDL Sea Ice Simulator (SIS) dynamic/thermodynamic sea ice model. The horizontal grid is that of the Geophysical Fluid Dynamics Laboratory Climate Model, version 2.6 (CM2.6; Delworth et al., 2012; Griffies et al., 2015); the horizontal grid spacing is $1/10^\circ$, corresponding to an effective horizontal grid spacing $\Delta \hat{\lambda} \approx 11$ km at the equator and decreasing with the cosine of latitude towards the poles. Southward of 65°S the latitudinal grid spacing is held constant at $\Delta y \approx 4.7$ km, whilst the longitudinal grid spacing continues to decrease to $\Delta x \approx 1.7$ km at 82°S . Northward of 65°N the grid is bipolar, displacing the poles over land so as to avoid the Δx singularity at the North Pole (Murray, 1996). This horizontal grid consists of 3600×2700 points. Bathymetry is interpolated onto the horizontal grid from the General Bathymetry Chart of the Oceans (GEBCO) 30 arc-second product, with the model incorporating the partial bottom cells scheme (Adcroft et al., 1997; Pacanowski and Gnanadesikan, 1998).

The model circulation is initialised from rest with the hydrographic conditions interpolated from the WOA13 climatology (Locarnini et al., 2013; Zweng et al., 2013) onto the GFDL50 vertical grid. This simulation is forced at the surface with the Coordinated Ocean Reference Experiment version 2 (CORE2) repeating climatological “normal” year forcing (Griffies et al., 2009; Large and Yeager, 2009). The model is run for a spin-up period of 45 years, at

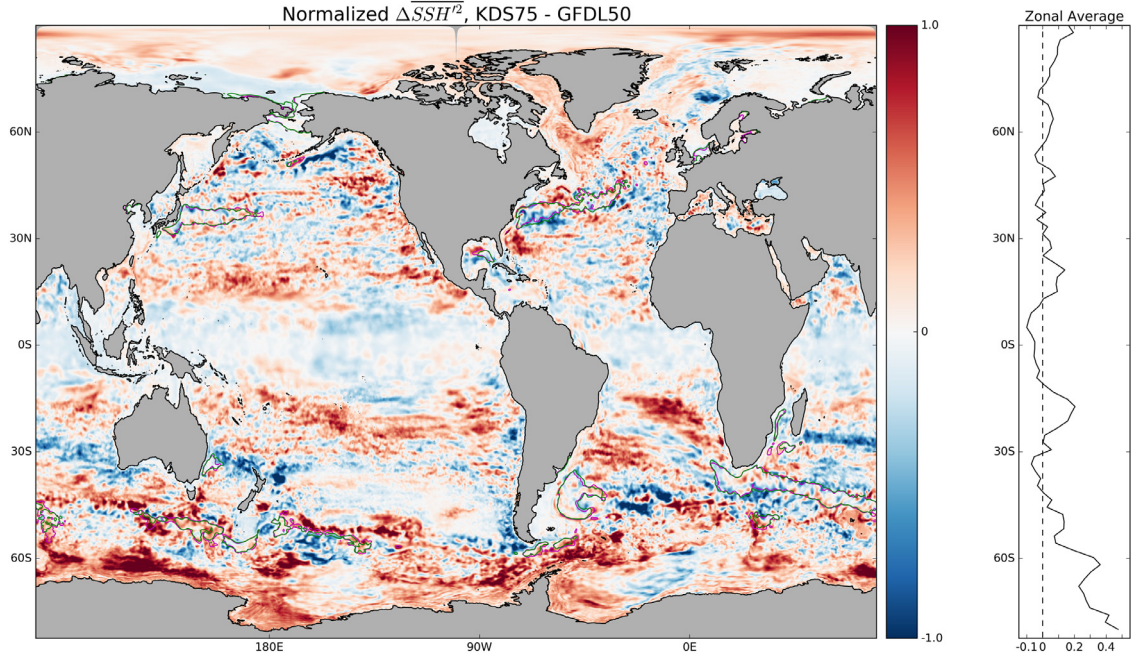


Fig. 9. The global distribution (left) and zonal average (right) of the normalized difference in daily SSH variance (m^2) between 10 years of the KDS75 and GFDL50 simulations. The red (blue) saturates in regions where the KDS75 (GFDL50) SSH variance is larger by more than the mean of the two simulations. Overall, the KDS75 simulation exhibits more SSH variability, especially in the mid- and high-latitudes. The green and magenta contours show regions where the $\overline{SSH}^2 > 0.015 \text{ m}^2$ for the GFDL50 and KDS75 simulations, respectively, indicating that the spatial distribution of the high-SSH variance regions are similar. (For interpretation of the references to colour in this figure legend, the reader is referred to the web version of this article.)

which time the hydrographic state is interpolated onto the KDS75 vertical grid, branching off the second simulation with improved vertical resolution. These two simulations are run in parallel for 20 years each (so that the GFDL50 run is now 65 years since initialisation, and the KDS75 run is 20 years since branching off the GFDL50 run). From this point the simulations are run for another 10 years, outputting their daily-averaged sea surface height (SSH) fields along with the seasonally-averaged meridional transport in potential density coordinates. For the final 5 years of each simulation, the daily-averaged 3D (u, v) fields are output for the region south of 30°S . These time-averaged diagnostics are calculated online by accumulating the respective fields at each timestep and saving their daily- and/or seasonal-averages.

4.1. Methodology

Given that the primary purpose of the vertical grid in global ocean models is to resolve the vertical structure of the horizontal flow, we focus the investigations on aspects of the horizontal flow known to be resolution-sensitive and have leading-order influences on the general circulation. These aspects include the variability associated with horizontal motions and the horizontal transport in potential density coordinates. The concurrent timeseries of the SSH, (u, v) and meridional transport in potential density coordinates enable the calculation and direct comparison of SSH variance, barotropic and baroclinic eddy kinetic energy (EKE_{BT} and EKE_{BC} , respectively) distributions, as well as the meridional overturning in density space. These are fields for which direct comparisons do not require completely equilibrated circulations, which are not yet available for these expensive simulations. The meridional overturning in particular is likely to be subject to long-term model drifts, which in turn may be different for the two vertical resolutions examined here, thereby influencing the model comparisons.

Here, the SSH variability is calculated with 10 years of daily SSH fields. First, the SSH annual cycle is determined (as the average SSH for each day of the year), temporally-smoothed with a 30-day

moving average, and then removed, leaving a 10-year daily record of de-seasoned SSH variation from the smoothed annual cycle. The variance of this field is then calculated for the two simulations; we examine the difference between these variances, normalized by the mean of the two simulations.

For the region south of 30°S we output 5 years of daily 3D (u, v) fields. These horizontal velocity fields are first de-seasoned by removing their annual cycle, and then decomposed into their barotropic (u_{BT}, v_{BT}) and baroclinic (u_{BC}, v_{BC}) components, as,

$$u(x, y, z, t) = u_{BT}(x, y, z, t) + u_{BC}(x, y, z, t), \quad (18)$$

where u_{BT} is the depth-averaged velocity, with an equivalent expression for v . These barotropic and baroclinic velocities can be further decomposed into their mean ($\overline{u_{BT}}$ and $\overline{u_{BC}}$, respectively) and eddy components (u'_{BT} and u'_{BC} , respectively), as,

$$u_{BT}(x, y, z, t) = \overline{u_{BT}}(x, y, z) + u'_{BT}(x, y, z, t), \quad (19)$$

and

$$u_{BC}(x, y, z, t) = \overline{u_{BC}}(x, y, z) + u'_{BC}(x, y, z, t), \quad (20)$$

where the eddy terms represent contributions from all transient flows. The timeseries of the eddy velocity fields (u'_{BT} and u'_{BC}) are used to calculate the 5-year mean of the barotropic and baroclinic eddy kinetic energies as,

$$\overline{EKE_{BT}}(x, y) = \frac{\overline{u'^2_{BT}} + \overline{v'^2_{BT}}}{2}, \quad (21)$$

and

$$\overline{EKE_{BC}}(x, y, z) = \frac{\overline{u'^2_{BC}} + \overline{v'^2_{BC}}}{2}, \quad (22)$$

respectively. We compare the differences of these EKE fields, again normalized by the relevant mean EKE of the two simulations.

The meridional overturning in potential density coordinates is diagnosed from the seasonally-averaged meridional horizontal transport within potential density classes. The 10-year mean of the

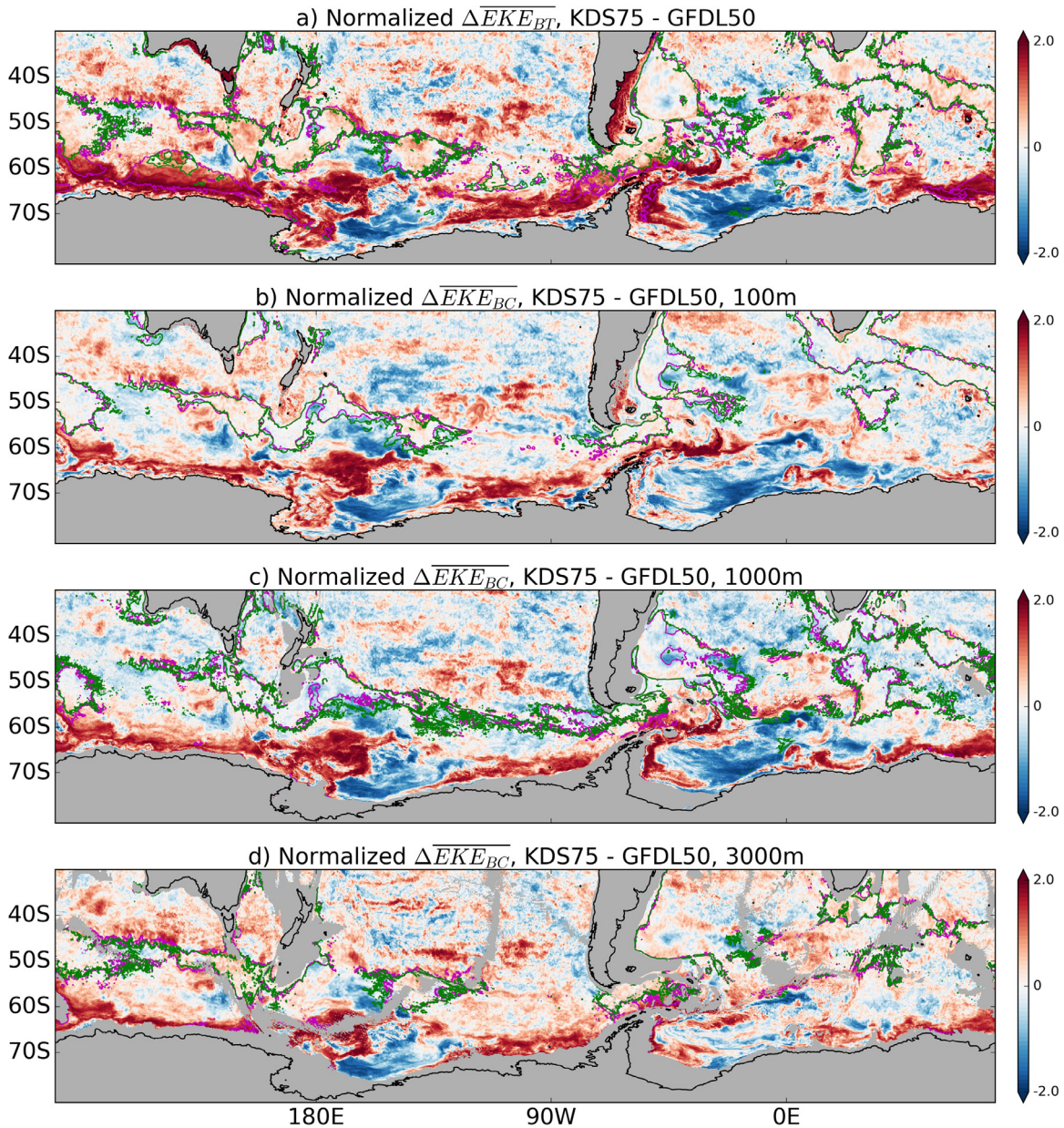


Fig. 10. The normalized difference in EKE (m^2s^{-2}) between 5 years of daily de-seasoned (u, v) fields of the KDS75 and GFDL50 simulations. The red (blue) saturates in regions where the KDS75 (GFDL50) EKE is larger by more than 200% of the two-simulation mean. The panels show the normalized differences of (a) the barotropic EKE_{BT} , and the baroclinic EKE_{BC} of the cells closest to (b) 100 m, (c) 1000 m, and (d) 3000 m depth. Contours indicate regions where the KDS75 (magenta) and GFDL50 (green) mean EKE is larger than (a) 10^{-3} , (b) 10^{-2} , and (c,d) $5 \times 10^{-4} m^2s^{-2}$. (For interpretation of the references to colour in this figure legend, the reader is referred to the web version of this article.)

zonally-integrated meridional overturning streamfunction in potential density space is calculated and compared for the two simulations. To gauge the effect of model drift on the results, we also performed these comparisons with the 1-year mean EKE , 5-year mean SSH variability, and 5-year mean meridional overturning circulation, which were found to be qualitatively consistent with the longer-term means presented here.

4.2. Modelling results

The direct comparison of the $1/10^\circ$ global simulations using the GFDL50 and KDS75 vertical grids provides a clear demonstration of the dynamical differences resulting from the improvement of vertical resolution. Vertical resolution has a strong influence on the de-seasoned SSH variance (Fig. 9). The KDS75 run exhibits substan-

tially more SSH variance in the mid- and high-latitudes, especially along the Antarctic continental shelf and slope. There is a slight decrease in SSH variance at the equator. The regions typically associated with large SSH variability (e.g., western boundary current separation points, topographic features within the Antarctic Circumpolar Current) are not dominant signals in the normalized SSH variance difference field; additionally, there is little difference between the respective locations of these high- SSH variance regions.

The Southern Ocean barotropic and baroclinic eddy kinetic energy (EKE_{BT} and EKE_{BC} , respectively) fields provide an opportunity to examine the vertical structure of the horizontal flow variability (Fig. 10). The general distribution of the normalized difference in EKE_{BT} has much in common with the normalized difference in SSH variance (compare Figs. 9 and 10a), although EKE_{BT} exhibits substantially more fine-scale structure. This is particularly the case

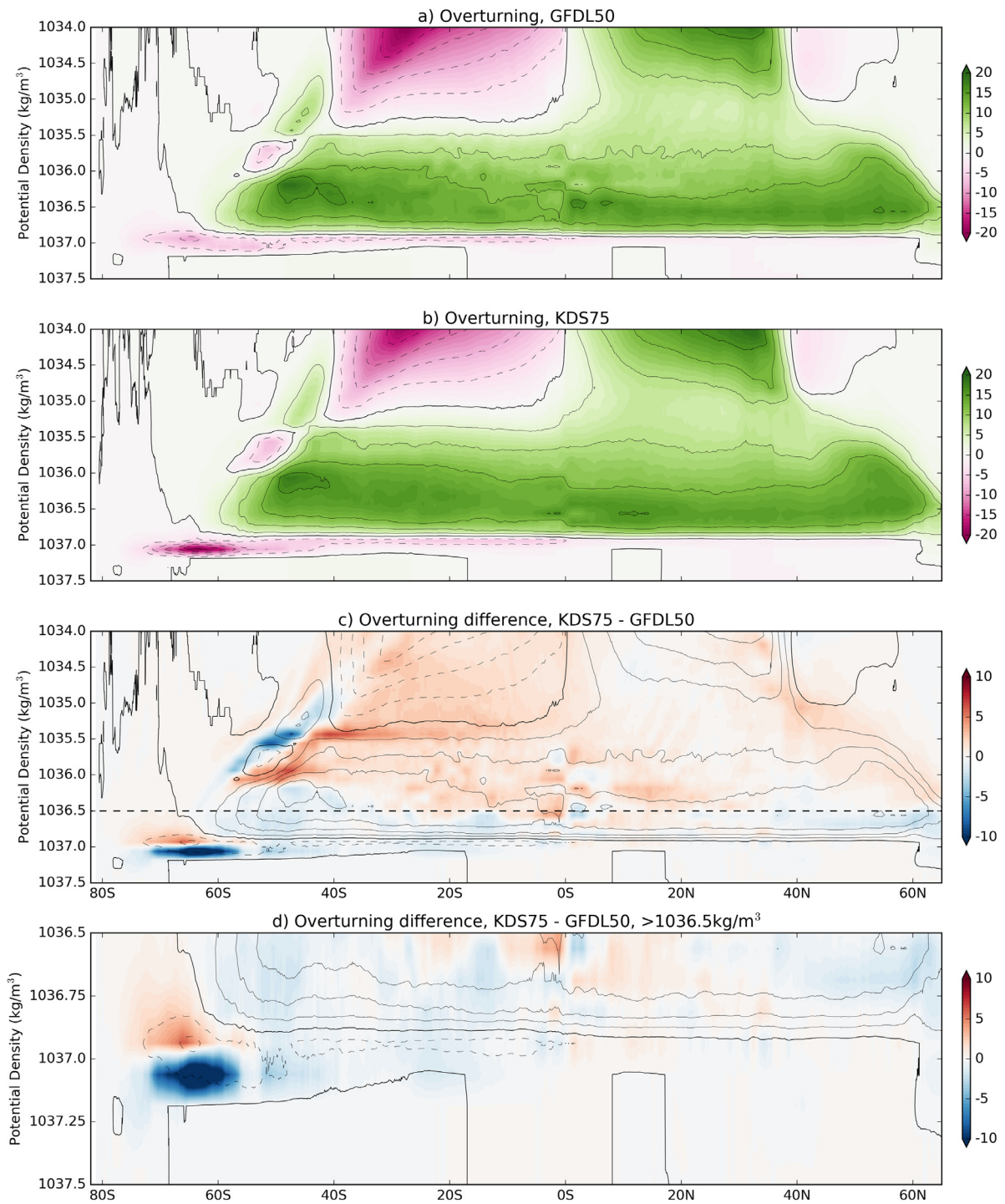


Fig. 11. The overturning streamfunctions (Sv) in potential density space for 10 years of the (a) GFDL50 and (b) KDS75 simulations, (c) the difference between them, and (d) focussing on the potential density range relevant for the AABW cell. The contours are at 4 Sv intervals, with the GFDL50 streamfunction contoured over the difference plots.

along the Antarctic continental shelf and slope. In general, the regions of relatively strong EKE (green and magenta contours) exhibit small normalized EKE differences; the exception to this is the EKE_{BT} on the Antarctic continental slope, which is relatively strong in the KDS75 simulation but not in the GFDL50. The comparison of baroclinic eddy kinetic energy shows the enhanced variability surrounding the Antarctic continental shelf and slope continues full-depth (Fig. 10b–d).

The increased SSH variability, EKE_{BT} and EKE_{BC} of the KDS75 simulation on and against the Antarctic continental shelf and slope,

especially along the eastern edge of the Antarctic Peninsula and the Ross Sea region, will likely facilitate enhanced formation, shelf-exchange and sinking of Antarctic Bottom Water (AABW) (e.g. Stewart and Thompson, 2013), for which models tend to exhibit a low bias in transport and density (e.g. Downes et al., 2011; Sallée et al., 2013; Downes et al., 2015; Farneti et al., 2015). This hypothesis can be tested by comparing the meridional overturning streamfunctions in potential density space (Fig. 11). Improving the vertical resolution results in a near-threefold increase in the overturning streamfunction of AABW cell, increasing from a maximum of ~ 8 Sv

in the GFDL50 simulation to over ~ 22 Sv in the KDS75. For context, observational studies estimate the southern bottom cell transport to range between ~ 13 – 22 Sv (e.g., Talley et al., 2003; Lumpkin and Speer, 2007). The deep southern cell of the KDS75 simulation also exhibits an increase in potential density.

These dynamical enhancements of the eddy energy and overturning resulting from the improvement of vertical resolution come at the expense of additional computational costs, which must be weighed against the benefits. The present-day practice for the parallel-computing of global ocean models involves partitioning the ocean horizontally into many sub-domains, each of which has the full number of vertical levels. This partitioning means that an increase in the number of vertical levels results in a linear increase in the computational load for both processing and storage, so that increasing the vertical levels from the GFDL50 to the KDS75 increases the computational load by 50%. It is well established that increases in SSH variance, EKE and overturning circulation equivalent to those presented here can be achieved by refining the horizontal resolution (e.g. Morrison and Hogg, 2013), representing a physically relevant improvement in the model circulation. However, unlike the linear relationship with the vertical resolution, the increase in computational load for refining horizontal resolution is at best quadratic (not including the additional costs associated with the reduced timestep required to maintain numerical stability), meaning the equivalent dynamical improvements will certainly come at a greater computational cost when relying on horizontal (not vertical) resolution enhancements.

5. Conclusion

The challenges presented by grid resolution will accompany global ocean modelling efforts into the foreseeable future. Objectively quantifying the vertical resolution requirements for global ocean models removes an important subjective element from the model configuration process. Here, we suggest that the principle purpose of the vertical grid is to resolve the vertical structure of the horizontal flows, which can be approximated by the baroclinic modal basis functions calculated from global hydrographic observations. Based on these functions we develop lower-bounds for the vertical grid spacing required to capture the baroclinic dynamics of a given mode, which is provided by the theoretical capabilities of the horizontal grid, and thereby ensuring the vertical grid supports the horizontal grid. With this approach we construct and compare vertical grids designed for use in high-resolution ($\sim 1/10^\circ$) z-coordinate global ocean models. It is found that at least 50 well-located vertical levels are required for a z-coordinate global ocean model to resolve the first baroclinic mode, with an additional 25 levels per subsequent mode. And while the methodology presented here is in an intuitive framework with direct application to z-coordinate ocean models, in principle it can be scaled to suit the vertical schemes of alternative layered-coordinate ocean models (i.e., terrain-following or isopycnal coordinate).

In addition to the observational-based comparison of the various vertical grids, we also present output from high-resolution ocean-sea ice simulations as a demonstration of the dynamical differences resulting from the vertical resolution improvement of a $1/10^\circ$ global ocean model. Improving the vertical resolution from a pre-existing 50 level grid to a new, objectively constructed 75 level grid results in a substantial increase in the sea surface height variance, especially in the Southern Ocean where the increase approaches 30%. The barotropic and baroclinic eddy kinetic energies also increase, with the spatial distribution of their differences largely reflecting that of the sea surface height analysis, and exhibiting increases of up to 200% on and surrounding the Antarctic continental shelf and slopes. The improved vertical resolution also results in an increase in the Antarctic Bottom Water formation

and overturning, exhibiting a near-tripling of the streamfunction in potential density space at 65°S . Arguably, equivalent increases in these dynamics could be achieved through further refining the horizontal resolution rather than the vertical, however such an exercise would attract considerably greater additional computation costs compared to those arising from the vertical resolution enhancement presented here.

Acknowledgments

The WOCE observational data were obtained from the Electronic Atlas of WOCE Data website, www.ewoce.org. The WOA13 climatology data were obtained from the NOAA website, www.nodc.noaa.gov. Many thanks to A. Adcroft, S. Downes, A. Gibson, R. Holmes, C. Shakespeare and A. Stewart for very helpful discussions, and to the COSIMA consortium (www.cosima.org.au) for making available the $1/10^\circ$ global model output. A.M.H., P.S. and M.H.E were supported by ARC Fellowships FT120100842, DE150100223 and FL100100214, respectively. The numerical simulations and analysis were performed with the resources of the National Computational Infrastructure (Canberra, Australia). The code for building the vertical grid is available at www.github.com/kialstewart. The authors would like to thank the anonymous reviewers for their valuable comments and suggestions to improve the quality of the paper.

References

- Adamec, D., 1988. Numerical simulations of the effects of seamounts and vertical resolution on strong ocean flows. *J. Phys. Oceanogr.* 18, 258–269.
- Adcroft, A., Hill, C., Marshall, J., 1997. Representation of topography by shaved cells in a height coordinate ocean model. *Mon. Weather Rev.* 125, 2293–2315.
- Barnier, B., Hua, B.L., Provost, C.L., 1991. On the catalytic role of high baroclinic modes in eddy-driven large-scale circulations. *J. Phys. Oceanogr.* 21, 976–997.
- Bernie, D.J., Woolnough, S.J., Slingo, J.M., Guilyardi, E., 2005. Modelling diurnal and intraseasonal variability of the ocean mixed layer. *J. Clim.* 18, 1190–1202.
- Brainerd, K.E., Gregg, M.C., 1993. Diurnal restratification and turbulence in the oceanic surface mixed layer: 1. Observations. *J. Geophys. Res.* 98, 22645–22656.
- Chassignet, E.P., Marshall, D.P., 2007. Gulf stream separation in numerical ocean models. In: Hecht, M., Hasumi, H. (Eds.), *Ocean Modelling in an Eddy Regime*. Geophysical Monograph Series, Vol. 177. American Geophysical Union, pp. 39–61.
- Chelton, D.B., DeSzoeke, R.A., Schlax, M.G., Naggar, K.E., Siwertz, N., 1998. Geographic variability of the first baroclinic Rossby radius of deformation. *J. Phys. Oceanogr.* 28, 433–460.
- Delworth, T.L., Rosati, A., Anderson, W., Adcroft, A.J., Balaji, V., Benson, R., Dixon, K., Griffies, S.M., Lee, H.C., Pacanowski, R.C., Vecchi, G.A., Wittenberg, A.T., Zeng, F., Zhang, R., 2012. Simulated climate and climate change in the GFDL CM2.5 high-resolution coupled climate model. *J. Clim.* 25, 2755–2781.
- Downes, S.M., Farneti, R., Uotila, P., Griffies, S.M., Marsland, S.J., Bailey, D., Behrens, E., Bentsen, M., Bi, D., Biastoch, A., Böning, C., Bozec, A., Canuto, V.M., Chassignet, E., Danabasoglu, G., Danilov, S., Diansky, N., Drange, H., Fogli, P.G., Gusev, A., Howard, A., Ilicak, M., Jung, T., Kelley, M., Large, W.G., Leboissetier, A., Long, M., Lu, J., Masina, S., Mishra, A., Navarra, A., Nurser, A.J.G., Patara, L., Samuels, B.L., Sidorenko, D., Spence, P., Tsujino, H., Wang, Q., Yeager, S.G., 2015. An assessment of Southern Ocean water masses and sea ice during 1988–2007 in a suite of interannual CORE-II simulations. *Ocean Modell.* 94, 67–94. doi:10.1016/j.ocemod.2015.07.022.
- Downes, S.M., Gnanadesikan, A., Griffies, S.M., Sarmiento, J.L., 2011. Water mass exchange in the Southern Ocean in coupled climate models. *J. Phys. Oceanogr.* 41, 1756–1771. doi:10.1175/2011JPO4586.1.
- Ducet, N., Traou, P.-Y.L., Reverdin, G., 2000. Global high-resolution mapping of ocean circulation from TOPEX/Poseidon and ERS-1 and -2. *J. Geophys. Res.* 105, 19477–19498. doi:10.1029/2000JC900063.
- Farneti, R., Downes, S.M., Griffies, S.M., Marsland, S.J., Behrens, E., Bentsen, M., Bi, D., Biastoch, A., Böning, C., Bozec, A., Canuto, V.M., Chassignet, E., Danabasoglu, G., Danilov, S., Diansky, N., Drange, H., Fogli, P.G., Gusev, A., Hallberg, R.W., Howard, A., Ilicak, M., Jung, T., Kelley, M., Large, W.G., Leboissetier, A., Long, M., Lu, J., Masina, S., Mishra, A., Navarra, A., Nurser, A.J.G., Patara, L., Samuels, B.L., Sidorenko, D., Tsujino, H., Uotila, P., Wang, Q., Yeager, S.G., 2015. An assessment of Antarctic circumpolar current and Southern Ocean meridional overturning circulation during 1958–2007 in a suite of interannual CORE-II simulations. *Ocean Modell.* 93, 84–120. doi:10.1016/j.ocemod.2015.07.009.
- Ferrari, R., Griffies, S.M., Nurser, A.J.G., Vallis, G.K., 2010. A boundary-value problem for the parameterized mesoscale eddy transport. *Ocean Modell.* 32, 143–156. doi:10.1016/j.ocemod.2010.01.004.
- Gayen, B., Griffiths, R.W., Hughes, G.O., Saenz, J.A., 2013. Energetics of horizontal convection. *J. Fluid Mech.* 716, doi:10.1017/JFM.2012.592. R10.

- Griffies, S.M., 2012. Elements of the Modular Ocean Model (MOM): 2013 Release. GFDL Ocean Group Technical Report, 7. NOAA/Geophysical Fluid Dynamics Laboratory, 614pp. [Available online at <http://www.mom-ocean.org/web/docs>].
- Griffies, S.M., Biastoch, A., Böning, C., Bryan, F., Danabasoglu, G., Chassignet, E.P., England, M.H., Gerdes, R., Haak, H., Hallberg, R.W., Hazeleger, W., Jungclauss, J., Large, W.G., Madec, G., Pirani, A., Samuels, B.L., Scheinert, M., Gupta, A.S., Severijns, C.A., Simmons, H.L., Treguier, A.M., Winton, M., Yeager, S., Yin, J., 2009. Coordinated ocean-ice reference experiments (COREs). *Ocean Modell.* 26, 1–46. doi:10.1016/j.ocemod.2008.08.007.
- Griffies, S.M., Böning, C., Bryan, F.O., Chassignet, E.P., Gerdes, R., Hasumi, H., Hirst, A., Treguier, A.M., Webb, D., 2000. Developments in ocean climate modelling. *Ocean Modell.* 2, 123–192.
- Griffies, S.M., Treguier, A.M., 2013. Ocean circulation models and modelling. In: Siedler, G., Griffies, S., Gould, J., Church, J. (Eds.), *Ocean Circulation and Climate: A 21st Century Perspective*, International Geophysics, Vol. 103. Elsevier, pp. 521–551.
- Griffies, S.M., Winton, M., Anderson, W.G., Benson, R., Delworth, T.L., Dufour, C.O., Dunne, J.P., Goddard, P., Morrison, A.K., Rosati, A., Wittenberg, A.T., Yin, J., Zhang, R., 2015. Impacts on ocean heat from transient mesoscale eddies in a hierarchy of climate models. *J. Clim.* 28, 952–977.
- The DRACKAR Group, 2007. Eddy-permitting ocean circulation hindcasts of past decades. *CLIVAR Exch.* 12, 3.
- Hallberg, R., 2013. Using a resolution function to regulate parameterizations of oceanic mesoscale eddy effects. *Ocean Modell.* 72, 92–103. doi:10.1016/j.ocemod.2013.08.007.
- Hallberg, R., Gnanadesikan, A., 2006. The role of eddies in determining the structure and response of the wind-driven southern hemisphere overturning: results from the modelling eddies in the Southern Ocean (MESO) project. *J. Phys. Oceanogr.* 36, 2232–2252. doi:10.1175/JPO2980.1.
- Hallberg, R., Rhines, P., 1996. Buoyancy-driven circulation in an ocean basin with isopycnals intersecting the sloping boundary. *J. Phys. Oceanogr.* 26, 913–940.
- Hewitt, H.T., Roberts, M.J., Hyder, P., Graham, T., Rae, J., Belcher, S.E., Bourdalle-Badie, R., Copsey, D., Coward, A., Guiavarch, C., Harris, C., Hill, R., Hirschi, J.J.-M., Madec, G., Mizielinski, M.S., Neinger, E., New, A.L., Rioual, J.-C., Sinha, B., Storkey, D., Shelly, A., Thorpe, L., Wood, R.A., 2016. The impacts of resolving the Rossby radius at mid-latitudes in the ocean: results from a high-resolution version of the met office GC2 coupled model. *Geosci. Model Dev. Discuss.* doi:10.5194/GMD-2016-87.
- Hill, C., Menemenlis, D., Ciotti, B., Henze, C., 2007. Investigating solution convergence in a global ocean model using a 2048-processor cluster of distributed shared memory machines. *Sci. Program.* 15, 107–115. doi:10.1155/2007/458463.
- Hunt, F.K., Tailleux, R., Hirschi, J.J.-M., 2012. The vertical structure of oceanic Rossby waves: a comparison of high-resolution model data to theoretical vertical structures. *Ocean Sci.* 8, 19–35. doi:10.5194/OS-8-19-2012.
- IOC, SCOR, IAPSO, 2010. The international thermodynamic equation of seawater–2010: calculation and use of thermodynamic properties. *Manuals and Guides* 56. Intergovernmental Oceanographic Commission, UNESCO, 196pp. [Available online at <http://unesdoc.unesco.org/images/0018/001881/188170e.pdf>].
- Large, W.G., Yeager, S., 2009. The global climatology of an interannually varying air-sea flux data set. *Clim. Dyn.* 33, 341–364. doi:10.1007/S00382-008-0441-3.
- Legg, S., 2012. Overflows and convectively driven flows. In: Chassignet, E., Cenedese, C., Verron, J. (Eds.), *Buoyancy-Driven Flows*. Cambridge University Press, pp. 203–239.
- Lindzen, R.S., Fox-Rabinovitz, M.S., 1989. Consistent vertical and horizontal resolution. *Mon. Weather Rev.* 117, 2575–2583.
- Locarnini, R.A., Mishonov, A.V., Antonov, J.I., Boyer, T.P., Garcia, H.E., Baranova, O.K., Zweng, M.M., Paver, C.R., Reagan, J.R., Johnson, D.R., Hamilton, M., Seidov, D., 2013. *World Ocean Atlas 2013, volume 1: temperature*. In: Levitus, S., Mishonov, A. (Eds.), *NOAA Atlas NESDIS 73*.
- Lumpkin, R., Speer, K., 2007. Global ocean meridional overturning. *J. Phys. Oceanogr.* 37, 2550–2562. doi:10.1175/JPO3130.1.
- MacKinnon, J., Laurent, L.S., Garabato, A.C.N., 2013. Diapycnal mixing processes in the ocean interior. In: Siedler, G., Griffies, S., Gould, J., Church, J. (Eds.), *Ocean Circulation and Climate: A 21st Century Perspective*, International Geophysics, Vol. 103. Elsevier, pp. 159–183.
- Madec, G., 2008. NEMO ocean engine. *Note du Pôle de Modélisation de l'Institut Pierre-Simon Laplace* 27.
- Mahadevan, A., 2006. Modelling vertical motion at ocean fronts: are nonhydrostatic effects relevant at submesoscales? *Ocean Modell.* 14, 222–240. doi:10.1016/j.ocemod.2006.05.005.
- Marshall, J., Adcroft, A., Hill, C., Perelman, L., Heisey, C., 1997. A finite-volume, incompressible Navier Stokes model for studies of the ocean on parallel computers. *J. Geophys. Res.* 102, 5753–5766. doi:10.1029/96JC02775.
- McWilliams, J.C., 2008. The nature and consequences of oceanic eddies. *Geophys. Monogr. Ser.* 177, 5–15. doi:10.1029/177GM03.
- Melet, A., Hallberg, R., Legg, S., Nikurashin, M., 2014. Sensitivity of the ocean state to lee wave-driven mixing. *J. Phys. Oceanogr.* 44, 900–921. doi:10.1175/JPO-D-13-072.1.
- Morrison, A.K., Hogg, A., 2013. On the relationship between Southern Ocean overturning and ACC transport. *J. Phys. Oceanogr.* 43, 140–148. doi:10.1175/JPO-D-12-057.1.
- Murray, R.J., 1996. Explicit generation of orthogonal grids for ocean models. *J. Comput. Phys.* 126, 251–273.
- Naveira Garabato, A.C., Polzin, K.L., King, B.A., Heywood, K.J., Visbeck, M., 2004. Widespread intense turbulent mixing in the Southern Ocean. *Science* 303, 210–213.
- Oke, P.R., Griffin, D.A., Schiller, A., Fiedler, R.J., Mansbridge, J.V., Lenton, A., Cahill, M., Chamberlain, M.A., Ridgway, K., 2012. Evaluation of a near-global eddy-resolving ocean model. *Geosci. Model Dev.* 6, 591–615. doi:10.5194/GMD-6-591-2013.
- Pacanowski, R.C., Gnanadesikan, A., 1998. Transient response in a 2-level ocean model that resolves topography with partial-cells. *Mon. Weather Rev.* 126, 3248–3270.
- Phillips, H.E., Bindoff, N.L., 2014. On the nonequivalent barotropic structure of the Antarctic circumpolar current: an observational perspective. *J. Geophys. Res.* 119, 5221–5243. doi:10.1002/2013JC009516.
- Rhines, P., 1970. Edge-, bottom-, and Rossby waves in a rotating stratified fluid. *Geophys. Fluid Dyn.* 1, 273–302.
- Rocha, C.B., Chereskin, T.K., Gille, S.T., Menemenlis, D., 2016. Mesoscale to submesoscale wavenumber spectra in Drake passage. *J. Phys. Oceanogr.* 46, 601–620. doi:10.1175/JPO-D-15-0087.1.
- Roeckner, E., Brokopf, R., Esch, M., Giorgetta, M., Hagemann, S., Kornblueh, L., Manzini, E., Schlese, U., Schulzweida, U., 2006. Sensitivity of simulated climate to horizontal and vertical resolution in the ECHAM5 atmosphere model. *J. Clim.* 19, 3771–3791. doi:10.1175/JCLI3824.1.
- Sallée, J.-B., Shuckburgh, E., Bruneau, N., Meijers, A.J.S., Bracegirdle, T.J., Wang, Z., Roy, T., 2013. Assessment of Southern Ocean water mass circulation and characteristics in CMIP5 models: historical bias and forcing response. *J. Geophys. Res.* 118, 1830–1844. doi:10.1002/JGRC.20135.
- Schlitzer, R., 2000. *Electronic atlas of WOCE hydrographic and tracer data now available*. *Eos Trans.* 81, 45.
- Schlitzer, R., 2015. Ocean data view. <http://odv.awi.de>.
- Smith, K.S., 2007. The geography of linear baroclinic instability in Earth's oceans. *J. Mar. Res.* 65, 655–683.
- Soufflet, Y., Marchesiello, P., Lemarié, F., Jouanno, J., Capet, X., Debreu, L., Benshila, R., 2016. On effective resolution in ocean models. *Ocean Modell.* 98, 36–50. doi:10.1016/j.ocemod.2015.12.004.
- Stewart, A.L., Thompson, A.F., 2013. Connecting antarctic cross-shelf exchange with Southern Ocean overturning. *J. Phys. Oceanogr.* 43, 1453–1471. doi:10.1175/JPO-D-12-0205.1.
- Stewart, K.D., Spence, P., Waterman, S., Sommer, J.L., Molines, J.-M., Lilly, J., England, M.H., 2015. Anisotropy of eddy variability in the global ocean. *Ocean Modell.* 95, 53–65. doi:10.1016/j.ocemod.2015.09.005.
- Tailleux, R., 2003. Comments on “the effect of bottom topography on the speed of long extratropical planetary waves”. *J. Phys. Oceanogr.* 33, 1536–1541.
- Talley, L.D., Reid, J.L., Robbins, P.E., 2003. Data-based meridional overturning streamfunctions for the global ocean. *J. Clim.* 16, 3213–3226.
- Thomas, L.N., Tandon, A., Mahadevan, A., 2007. Submesoscale processes and dynamics. In: Hecht, M., Hasumi, H. (Eds.), *Ocean Modelling in an Eddy Regime*, Geophysical Monograph Series, Vol. 177. American Geophysical Union, pp. 17–38.
- Treguier, A.M., Dukowicz, J.K., Bryan, K., 1996. Properties of nonuniform grids used in ocean general circulation models. *J. Geophys. Res.* 101, 20877–20881.
- Waterman, S., Hogg, N.G., Jayne, S.R., 2011. Eddy-mean flow interactions in the Kuroshio extension region. *J. Phys. Oceanogr.* 41, 1182–1208. doi:10.1175/2010JP04564.1.
- Weaver, A.J., Sarachik, E.S., 1990. On the importance of vertical resolution in certain ocean general circulation models. *J. Phys. Oceanogr.* 20, 600–609.
- Wunsch, C., 1997. The vertical partition of oceanic horizontal kinetic energy. *J. Phys. Oceanogr.* 27, 1770–1794.
- Wunsch, C., 2007. The past and future ocean circulation from a contemporary perspective. In: *Ocean Circulation: Mechanisms and Impacts*, Geophysical Monograph Series, Vol. 173. American Geophysical Union, pp. 53–74. doi:10.1029/173GM06.
- Zweng, M.M., Reagan, J.R., Antonov, J.I., Locarnini, R.A., Mishonov, A.V., Boyer, T.P., Garcia, H.E., Baranova, O.K., Paver, C.R., Johnson, D.R., Seidov, D., Biddle, M., 2013. *World Ocean Atlas 2013, volume 2: salinity*. In: Levitus, S., Mishonov, A. (Eds.), *NOAA Atlas NESDIS 74*.